Phase resonance testing of highly flexible structures: Measurement of conservative nonlinear modes and nonlinear damping identification

Marielle Debeurre [a], Simon Benacchio [a], Aurélien Grolet [a], Clément Grenat [c], Christophe Giraud-Audine [b], Olivier Thomas [a,*]

[a] *Arts et Métiers Institute of Technology, LISPEN, HESAM Université, F-59000 Lille, France*
[b] *Arts et Métiers Institute of Technology, L2EP, HESAM Université, Univ. Lille, Centrale Lille, JUNIA, F-59000 Lille, France*
[c] *Framatome, 1 Pl. Coupole Jean Millier, 92400 Courbevoie, France*

ABSTRACT

This article addresses the measurement of the nonlinear modes of highly flexible structures vibrating at extreme amplitude, using a Phase-Locked Loop experimental continuation technique. By separating the motion into its conservative and dissipative parts, it is theoretically proven for the first time that phase resonance testing organically allows for measurement of the conservative nonlinear modes of a structure, whatever be its damping law, linear or nonlinear. This result is experimentally validated by measuring the first three nonlinear modes of a cantilever beam. Extreme amplitudes of motion (of the order of 120° of cross section rotation for the first mode) are reached for the first time, in air with atmospheric pressure condition, responsible for a strong nonlinear damping due to aeroelastic drag. The experimental backbone curves are validated through comparison to the conservative backbone curves obtained by numerical computations, with an excellent agreement. The classical trends of cantilever beams are recovered: a hardening effect on the first nonlinear mode and softening on the other modes. The nonlinear mode shapes are also measured and compared to their theoretical counterparts using camera capture. Finally, it is shown that the damping law can be estimated as a by-product of the phase resonance measurement of the conservative nonlinear modes. As an original result, the damping law is observed to be highly nonlinear, with quadratic and cubic evolutions as a function of the structure's amplitude.

1. Introduction

Highly flexible slender structures, with a characteristic length that greatly exceeds the dimensions of the cross section, often exhibit complex nonlinear behaviors in dynamics due to their very low stiffness in bending that allows the structures to deform at very large amplitudes [1–4]. Example applications of these types of structures include cables, cable bundles, hoses, wires, ropes, slender blades and wings, which are commonly found in the automotive [5,6], aerospace [7–10], electronic (micro- and nano-electromechanical systems) [11,12] industries, in energy harvesting applications [13–15], to design vibration absorbers [16] or in musical acoustics [17]. In this context, this article addresses the careful measurement of the nonlinear modes of cantilever beams at extreme vibration amplitudes, using Phase-Locked Loop experimental continuation.

Efficient simulation of the nonlinear dynamics of highly flexible structures at very large amplitudes of motion remains a challenge, in particular in the frequency domain where reliable and efficient numerical methods have been only recently developed [18–21]. In large amplitude experiments, the cantilever beam is in particular often considered since the boundary conditions allow for the dynamics to be measured at very large amplitudes with only moderate input forces. Despite the apparent simplicity of these structures, they can manifest complex nonlinear dynamics, including bending/torsion coupling [1,22], strong energy transfers between widely spaced modes [2,23–25], and aeroelastic drag damping [4]. Although those phenomena can be observed for moderate amplitudes of motion (on the order of maximum cross section rotations of 30° at the cantilever tip), the resonant response in very large amplitude motion was measured only recently in [21,26], in vacuum, up to rotations of 120° at the tip of the cantilever. In the present work, similar vibration cases are considered, but a method to carefully measure the nonlinear modes of these structures, *i.e.* the backbone curves, in addition to the nonlinear frequency responses and the nonlinear mode shapes is proposed, up to similar extreme amplitudes. Since the measurements of this work are performed in standard (non-vacuum) conditions, the damping effect of the air, essentially nonlinear, is significant and implies the use of standard phase resonance testing for computation of the nonlinear modes and nonlinear frequency responses.

The nonlinear modes of an elastic system have been given several definitions in the literature. In this work, the *conservative nonlinear modes* (CNMs) are considered, alternatively defined as periodic solutions of the conservative system in free vibration or as invariant manifolds of the phase space [27–30]. The CNMs provide a useful framework for the study of nonlinear dynamics as they efficiently map the frequency response of a multimode system with the *backbone curve*, thereby giving with only a single computation/measurement the nonlinear resonances and thus the skeleton of the dynamics in an amplitude/frequency plot. Numerical computation of nonlinear modes has been developed extensively in recent decades [27,31,32], but equivalent robust strategies for experimental measurement have only been investigated very recently. In [33], a method for the experimental measurement of the backbone curves was outlined, based on the idea of *phase resonance*. In order to measure the CNMs experimentally (where dissipative and external forces are present), a phase lag is imposed between the forcing and the response of the system. At this precise phase lag (*i.e.* at phase resonance), the forcing exactly cancels the energy dissipation due to damping, thus making the system behave as if in a free and conservative motion and thereby enabling measurement of its CNMs. Several experimental works have applied these principles to measure the experimental nonlinear modes [34–37] using a Phase-Locked Loop (PLL) controller to prescribe a given phase so as to develop an efficient and complete experimental characterization strategy (frequency responses and nonlinear modes) of nonlinear systems [34,38–40], even in the presence of internal resonances [41,42]. Damped nonlinear modes also exist [43,44], but are not the focus of the present work. In addition, the PLL is part of a larger family of experimental continuation methods [36,40,45–47], likewise outside of the focus of the present work.

In this context, the first goal of this article is to propose an experimental investigation and validation of the geometrically exact model of [18,19] for the simulation of highly flexible structures. To this end, we focus on the measurement of the backbone curves and the nonlinear mode shapes of the first three modes of a cantilever beam at very large amplitude, up to rotations angles of 120° at the tip for the first mode. The second goal of the present study is to apply a PLL-based experimental continuation technique to this problem in order to measure the nonlinear frequency response curves as well as the backbone curves with the concept of phase resonance. Since open-air experiments are considered in this work, several sources of damping may intervene (*e.g.* internal material damping, aeroelastic drag) in a complex manner, rendered even more complex since these effects can mix with the geometrical nonlinearities. As such, the third goal of the article consists in revisiting the standard phase resonance concept to include an arbitrary form of dissipative forces. In this work, we aim to prove with theory and demonstrate with experiments that with a properly applied phase resonance condition, a *conservative* nonlinear mode (backbone curve) is measured, *whatever be the dissipative forces* that come into play. Finally, a fourth goal is to demonstrate that an *estimation of the damping law* is possible during the process by monitoring the external forcing as a function of the amplitude of motion of the structure.

The study begins in Section 2 with a complete theoretical background and justification of the use of phase resonance to measure conservative nonlinear modes. In Section 3, the numerical computation of conservative nonlinear modes using phase resonance is investigated. The experiments involving vibration control of highly flexible structures and details on the PLL controller are presented in Section 4. Finally, the results of the experiments are compared to theory in Section 5, before concluding in Section 6.

2. Phase resonance & conservative nonlinear modes

2.1. Class of models

Consider a nonlinear system that is modeled by the following N-dimensional problem ($N \in \mathbb{N}$):

$$\boldsymbol{M}(\boldsymbol{x})\ddot{\boldsymbol{x}} + \boldsymbol{f}_\mathrm{d}(\boldsymbol{x}, \dot{\boldsymbol{x}}) + \boldsymbol{f}_\mathrm{c}(\boldsymbol{x}, \dot{\boldsymbol{x}}) = \boldsymbol{f}_\mathrm{e}, \tag{1}$$

where $\boldsymbol{x}(t)$ is the N-dimensional displacement vector, a function of time t, $\dot{\diamond} = \mathrm{d}\diamond/\mathrm{d}t$, $\boldsymbol{M}(\boldsymbol{x})$ is the $N \times N$ inertia matrix which may depend on $\boldsymbol{x}$ because of inertial nonlinearities, $\boldsymbol{f}_\mathrm{d}(\dot{\boldsymbol{x}}, \boldsymbol{x})$ is the N-dimensional dissipative force vector that depends on the velocity $\dot{\boldsymbol{x}}$ and on the displacement $\boldsymbol{x}$, $\boldsymbol{f}_\mathrm{c}(\boldsymbol{x}, \dot{\boldsymbol{x}})$ is the N-dimensional internal conservative force vector that depends on $\boldsymbol{x}$ and on $\dot{\boldsymbol{x}}$ in the case of inertial nonlinearities, and $\boldsymbol{f}_\mathrm{e}(t)$ is the N-dimensional external force vector that depends on time. Eq. (1) is very general and well-suited for modeling several types of systems. As shown in what follows, it can first be applied to a mechanical elastic structure subjected to geometrical nonlinearities and discretized either using a Galerkin method or a finite element (FE) method [30]. It can also be applied to model a multibody system without constraints [48]. Gyroscopic forces, that lead to a skew-symmetric operator and appear in particular in rotating systems [49], are not considered in this work.

The inertia term $\boldsymbol{M}(\boldsymbol{x})\ddot{\boldsymbol{x}}$ and the force vector $\boldsymbol{f}_{\mathrm{c}}$ gather all the *conservative* contributions in the model. The latter include all elastic forces and, in some cases, nonlinear inertial forces, leading to its possible dependence on the velocity. For illustration, consider the two classical main families of geometrically nonlinear structures (see *e.g.* [18,30]). The first family gathers structures for which the membrane behavior is constrained, either by boundary conditions (beams with restrained ends [50,51]) or because of 2D membrane effects (such as plates or shells [52–54]). In this case, the von Kármán family of models leads to a $\boldsymbol{f}_{\mathrm{c}}(\boldsymbol{x})$ which is a third order polynomial in $\boldsymbol{x}$ and does not depend on $\dot{\boldsymbol{x}}$. The second family of models gathers highly flexible structures such as cantilevers, rings, tree-like beam structures, ribbons, *etc.* (see [18,55]), for which the deformation of the centerline can reach very large amplitudes, such that the structures can be subjected to very large rotations of the cross sections for moderate external forces. In this case, $\boldsymbol{f}_{\mathrm{c}}(\boldsymbol{x})$ includes trigonometric functions of $\boldsymbol{x}$ (as in [18]). This model can be truncated to the third order in the transverse displacement and discretized with a Galerkin procedure, leading to inertial nonlinearities. These inertial nonlinearities, classical for multibody systems (see an example in Appendix A.1), lead to a mass matrix $\boldsymbol{M}(\boldsymbol{x})$ quadratic in $\boldsymbol{x}$ and an internal force vector $\boldsymbol{f}_{\mathrm{c}}(\boldsymbol{x},\dot{\boldsymbol{x}})$ quadratic in $\dot{\boldsymbol{x}}$, in addition to $\boldsymbol{f}_{\mathrm{c}}(\boldsymbol{x},\dot{\boldsymbol{x}})$ being cubic in $\boldsymbol{x}$ (see [7,56] and Appendix A.2). If three-dimensional finite elements are used, $\boldsymbol{f}_{\mathrm{c}}(\boldsymbol{x})$ is a third order polynomial in $\boldsymbol{x}$ in any case [57,58]. The conservative character of $\boldsymbol{f}_{\mathrm{c}}(\boldsymbol{x})$ is a consequence of a potential energy (for the elastic forces) and a kinetic energy (for the inertial forces).

The force vector $\boldsymbol{f}_{\mathrm{d}}$ gathers all *non conservative* contributions responsible for the damping of the oscillations. In the simplest case, this term takes the form of a linear viscous damping $\boldsymbol{f}_{\mathrm{d}} = \boldsymbol{D}\dot{\boldsymbol{x}}$ with $\boldsymbol{D}$ a $N \times N$ constant matrix. However, $\boldsymbol{f}_{\mathrm{d}}$ can also be nonlinear due to several different causes. For example, friction forces lead to a nonlinear damping which can be modeled with various contact laws, the simplest being a Coulomb model, intrinsically non-smooth (see *e.g.* [59]). Aeroelastic drag forces are often modeled with quadratic terms in $\dot{\boldsymbol{x}}$ (see [4] and Appendix A.3). Nonlinear damping can also be caused by internal dissipation in the form of viscoelastic forces that are nonlinear because of the geometrical nonlinearities, in which case $\boldsymbol{f}_{\mathrm{d}}$ becomes $\boldsymbol{f}_{\mathrm{d}} = \boldsymbol{D}(\boldsymbol{x})\dot{\boldsymbol{x}}$ with $\boldsymbol{D}$ quadratic in $\boldsymbol{x}$ (see [21,60] and Appendix A.2). Finally, special materials such as piezoelectric also manifest nonlinear dissipation forces (see [61] and Appendix A.4).

As described in the following sections, the present work focuses on systems that can be modeled by Eq. (1) where $\boldsymbol{M}(\boldsymbol{x})$, $\boldsymbol{f}_{\mathrm{d}}(\boldsymbol{x},\dot{\boldsymbol{x}})$ and $\boldsymbol{f}_{\mathrm{c}}(\boldsymbol{x},\dot{\boldsymbol{x}})$ are smooth functions of $\boldsymbol{x}$ and $\dot{\boldsymbol{x}}$. This *a priori* excludes for example the case of contact forces, which are intrinsically non-smooth. The distinction between $\boldsymbol{f}_{\mathrm{c}}$ and $\boldsymbol{f}_{\mathrm{d}}$ and some important properties is clarified in what follows.

2.2. Conservative nonlinear modes

Considering the nonlinear problem Eq. (1), it is common to define its nonlinear modes as an extension to the nonlinear range of the "linear" eigenmodes of the underlying linear and undamped system, the latter being defined by the pairs of eigenfrequencies/eigenshapes $(\omega_i, \boldsymbol{\Phi}_i)$, $i = 1, \dots, N$, solutions of:

$$\left[\boldsymbol{K} - \omega^2 \boldsymbol{M}(\boldsymbol{0})\right] \boldsymbol{\Phi} = \boldsymbol{0}, \quad \boldsymbol{K} = \left.\frac{\partial \boldsymbol{f}_{\mathrm{c}}}{\partial \boldsymbol{x}}\right|_{(\boldsymbol{x},\dot{\boldsymbol{x}})=(\boldsymbol{0},\boldsymbol{0})}, \tag{2}$$

with $\boldsymbol{K}$ the stiffness matrix and where the equilibrium point of the system is assumed as $(\boldsymbol{x}, \dot{\boldsymbol{x}}) = (\boldsymbol{0}, \boldsymbol{0})$. The *conservative nonlinear modes* (CNMs)[1] are then defined as particular solutions $\boldsymbol{x}_{\mathrm{cnm}}(t)$ of the undamped nonlinear problem Eq. (1) in free vibration:

$$\boldsymbol{M}(\boldsymbol{x}_{\mathrm{cnm}})\ddot{\boldsymbol{x}}_{\mathrm{cnm}} + \boldsymbol{f}_{\mathrm{c}}(\boldsymbol{x}_{\mathrm{cnm}}, \dot{\boldsymbol{x}}_{\mathrm{cnm}}) = \boldsymbol{0}, \tag{3}$$

and have two equivalent definitions. The CNMs can be defined (i) as invariant manifolds of the phase space [28,29] or (ii) as families of periodic solutions of Eq. (3) [27]. The two definitions are equivalent since any motion initiated on a periodic orbit remains in this periodic orbit and thus lies in an invariant manifold of the phase space. More theoretically, their existence is proven by a theorem of Lyapunov [65], which states that, with no internal resonance, there exist N two-dimensional CNMs in the phase space that emerge from the equilibrium point and are tangent to the N eigenplanes at this point. They are sometimes called Lyapunov Subcenter Manifolds (LSM) since their union is the center manifold [66,67]. In the same way as for the eigenmodes of the linear underlying system $(\omega_i, \boldsymbol{\Phi}_i)$, a CNM is characterized by a fundamental angular frequency ω and a deformed shape $\boldsymbol{x}_{\mathrm{cnm}}(t)$ which are functions of the amplitude of the motion. Plotting ω as a function of the amplitude leads to the *backbone curve* of the CNM.

It is also possible to define nonlinear modes of the damped system, *i.e.* solutions of Eq. (1) in free vibration (with $\boldsymbol{f}_{\mathrm{e}} = \boldsymbol{0}$). Contrary to the CNM, several nonequivalent definitions coexist, proposed by several authors independently to fulfill a given requirement. For model reduction purposes, the invariant manifold definition still exists for the case of damping and smooth nonlinearities [30,63,64,68]. For non-smooth nonlinearities, mainly for applications with friction damping, damped nonlinear modes have been defined in order to compute the skeleton of frequency responses as well as for model identification. A first definition for these damped nonlinear modes is a family of pseudo-periodic motions, obtained with a Fourier-Galerkin expansion of the dynamics [44]. Another definition is a family of periodic solutions of the homogeneous version of Eq. (3), where a fictitious negative linear damping term is added [35,43].

In practice, nonlinear modes are of great interest for the same reasons as the eigenmodes of the linear underlying system. They define the nonlinear resonances of the system, being the skeleton of its frequency response, and are thus an efficient way to

---

[1] Other terminologies in the literature are Nonlinear Normal Mode (NNM) and Lyapunov Subcenter Manifold (LSM). We choose to use the CNM terminology here in order to avoid the term "normal" initially brought by Rosenberg [62] and which is sometimes synonymous with "orthogonal," which is not appropriate for a nonlinear mode. A NNM can also be a nonlinear mode of the damped system in some texts [63,64]. We also choose not to use the "LSM" terminology since we prefer to use the "Nonlinear Mode" terminology, which is closer to the perspective of a structural mechanics engineer.

summarize the main dynamical characteristic of a system [27,69]. They can also be used for system identification [34]. In addition, nonlinear modes are of great importance in defining accurate reduced order models of the system [29,30]. Here, we focus on CNMs as there is no ambiguity in their definition. They are useful in the study of geometrically nonlinear structures for which the damping is typically weak, such that the conservative backbone curves lie very close to the resonances of the damped and forced system [67,69].

2.3. Monophase conservative nonlinear mode

If no internal resonance is activated, it is often observed (and introduced in the literature without theoretical proof) that a given CNM $x_{\mathrm{cnm}}(t)$ is periodic and monophase [33]. It is defined as:

$$x_{\mathrm{cnm}}(t) \simeq \hat{x}_0 + \sum_{h=1}^{H} \hat{x}_h \cos(h\omega t), \tag{4}$$

where the above (real) Fourier series has been truncated to H harmonics and with $\hat{x}_h \in \mathbb{R}^N$, $h \in \mathbb{N}$ defining the amplitude vector of the hth harmonic and ω the fundamental angular frequency.

In what follows, this monophase property is addressed and a theoretical justification is proposed. The CNM is the natural extension of the "linear" mode shape $\boldsymbol{\Phi}_i$ of the ith mode when the amplitude grows and thus when the motion on the invariant manifold moves away from the origin. The motion on the ith "linear" mode shape, valid close to the equilibrium point, is considered as:

$$x_{\mathrm{lm}}(t) = a\boldsymbol{\Phi}_i \cos \omega_i t, \tag{5}$$

with $a \in \mathbb{R}$ the amplitude. Eq. (5) is equivalent to imposing $\omega = \omega_i$, $\hat{x}_1 = a\boldsymbol{\Phi}_i$ and $\hat{x}_h = \boldsymbol{0}$ for $h \neq 1$ in Eq. (4). It is assumed that the conservative force vector $\boldsymbol{f}_{\mathrm{c}}(x, \dot{x})$ and the mass matrix $\boldsymbol{M}(x)$ are smooth around the equilibrium point $(x, \dot{x}) = (\boldsymbol{0}, \boldsymbol{0})$ and that $\boldsymbol{f}_{\mathrm{c}}(x, \dot{x})$ is an even function of $\dot{x}$ (this second property will be addressed in Section 2.4). Inserting the linear modal motion Eq. (5) into Eq. (3), it can be shown (see Appendix C) that the conservative forces are also monophase:

$$\boldsymbol{M}(x_{\mathrm{lm}})\ddot{x}_{\mathrm{lm}} + \boldsymbol{f}_{\mathrm{c}}(x_{\mathrm{lm}}, \dot{x}_{\mathrm{lm}}) = \hat{\boldsymbol{f}}_{\mathrm{c}0} + \sum_{h=1}^{H} \hat{\boldsymbol{f}}_{\mathrm{c}h} \cos(h\omega t), \tag{6}$$

where $\hat{\boldsymbol{f}}_{\mathrm{c}h} \in \mathbb{R}^N$. The nonlinearities in the conservative part of Eq. (1), then, naturally create harmonics that are only in phase with one another. The balancing of harmonics in Eq. (3) thus proves that the monophase CNM of Eq. (4) is an *admissible and natural solution*. It is the simplest form that can be obtained for a CNM and is characteristic of the main part of a backbone curve, away from the internal resonances branches, sometimes called "tongues" or "offshoots" [18,27]. At locations on the backbone curve of internal resonance tongues, this solution is still admissible in some cases: in Appendix D, it is shown through an example that the CNM remains monophase in a 1:3 internal resonance branch, but has components in quadrature for a 1:2 branch which emanates from the main branch because of symmetry-breaking bifurcations. In cases of internal resonance at low amplitude, when the "linear" natural frequencies are tuned, some phase quadrature between the components of x_{cnm} can be observed, resulting in non-monophase modes (referring to [41,70], Appendix D shows that for a 1:1 internal resonance, the "normal" coupled modes of a 1:1 internal resonance are monophase whereas the "elliptic modes" have some components in phase quadrature, as with the "parabolic modes" of a 1:2 internal resonance which likewise have components in phase quadrature).

The monophase form of the CNM (Eq. (4)) can be simplified further if there are symmetries in the system, *e.g.* for plates and straight beam structures where the transverse motion is symmetrical. In this case, the components of x_{cnm} related to the bending motion contain only odd harmonics, and those related to the axial/membrane motion contain only even harmonics (see Appendix F). This property is no longer valid in the case of symmetry-breaking bifurcations, meaning that asymmetric responses can also be solutions to a symmetric system.

2.4. Separation of conservative and dissipative parts

In this section, the dependence of the two force vectors $\boldsymbol{f}_{\mathrm{d}}(x, \dot{x})$ and $\boldsymbol{f}_{\mathrm{c}}(x, \dot{x})$ of Eq. (1) on the velocity $\dot{x}$ is addressed, depending on their conservative or non-conservative nature. First, the two vectors are gathered into a single internal force vector: $\boldsymbol{f} = \boldsymbol{f}_{\mathrm{d}} + \boldsymbol{f}_{\mathrm{c}}$. Then, following ideas from [33,71], $\boldsymbol{f}$ is decomposed into symmetric $\boldsymbol{f}_{\mathrm{s}}$ and antisymmetric $\boldsymbol{f}_{\mathrm{a}}$ functions of $\dot{x}$:

$$\boldsymbol{f} = \boldsymbol{f}_{\mathrm{s}} + \boldsymbol{f}_{\mathrm{a}}, \quad \text{with} \quad \begin{cases} \boldsymbol{f}_{\mathrm{s}}(x, \dot{x}) = \boldsymbol{f}_{\mathrm{s}}(x, -\dot{x}) = [\boldsymbol{f}(x, \dot{x}) + \boldsymbol{f}(x, -\dot{x})]/2, \\ \boldsymbol{f}_{\mathrm{a}}(x, \dot{x}) = -\boldsymbol{f}_{\mathrm{a}}(x, -\dot{x}) = [\boldsymbol{f}(x, \dot{x}) - \boldsymbol{f}(x, -\dot{x})]/2. \end{cases} \tag{7}$$

To analyze the conservative (or non-conservative) nature of $\boldsymbol{f}$, its work is computed over one period $T = 2\pi/\omega$ of a periodic motion:

$$\mathcal{W} = \int_{-T/2}^{T/2} \dot{x}^{\mathrm{T}} \boldsymbol{f}(x, \dot{x}) \, \mathrm{d}t = \int_{0}^{T/2} \dot{x}(t)^{\mathrm{T}} \boldsymbol{f}[x(t), \dot{x}(t)] \, \mathrm{d}t - \int_{0}^{T/2} \dot{x}(-t)^{\mathrm{T}} \boldsymbol{f}[x(-t), \dot{x}(-t)] \, \mathrm{d}t. \tag{8}$$

If a monophase CNM motion is chosen for the displacement vector such that $x(t) = x_{\mathrm{cnm}}(t)$ of Eq. (4), x is an even function of t ($x(t) = x(-t)$) and the velocity $\dot{x}$ is an odd function of t ($\dot{x}(t) = -\dot{x}(-t)$). Then, Eq. (8) becomes:

$$\mathcal{W} = \int_{0}^{T/2} \dot{x}(t)^{\mathrm{T}} \boldsymbol{f}[x(t), \dot{x}(t)] \, \mathrm{d}t - \int_{0}^{T/2} \dot{x}(t)^{\mathrm{T}} \boldsymbol{f}[x(t), -\dot{x}(t)] \, \mathrm{d}t. \tag{9}$$

Introducing the split of f according to Eq. (7), it can be shown that:

$$\mathcal{W} = \mathcal{W}_s + \mathcal{W}_a, \quad \text{with} \quad \left\{ \begin{array}{l} \mathcal{W}_s = 0, \\ \mathcal{W}_a = 2 \int_0^{T/2} \dot{x}(t)^{\mathrm{T}} f_a[x(t), \dot{x}(t)] \, \mathrm{d}t. \end{array} \right. \tag{10}$$

This demonstration shows that the work $\mathcal{W}_s$ of the symmetric part f_s on a monophase CNM is zero, indicating that f_s is a conservative force, whereas the work $\mathcal{W}_a$ is *a priori* non-zero, indicating that f_a is a non-conservative force. Then, the following property can be postulated: *whatever be the x dependence of the internal force $f(x, \dot{x})$, its conservative part $f_c(x, \dot{x})$ is an even function of $\dot{x}$ whereas its non-conservative part $f_d(x, \dot{x})$ is an odd function of $\dot{x}$.* Consequently:

$$\left\{ \begin{array}{l} f_c(x, \dot{x}) = f_c(x, -\dot{x}), \\ f_d(x, \dot{x}) = -f_d(x, -\dot{x}). \end{array} \right. \tag{11}$$

Even if the assumptions of the demonstration of this section appear restrictive, these results can be verified for most available damping models, linear or nonlinear, as shown in Appendix A on a selection of representative models.

2.5. Phase resonance

Consider now the system under forced and damped conditions, where the motion is described by Eq. (1). If the motion is exactly the monophase CNM of Eq. (4), it takes the form of Eq. (3) such that the conservative terms of Eq. (1) balance each other. In this case, Eq. (1) reduces to:

$$f_d(x_{\mathrm{cnm}}, \dot{x}_{\mathrm{cnm}}) = f_e = \sum_{h=1}^{H} -\hat{f}_{eh} \sin(h\omega t), \tag{12}$$

with $\hat{f}_{eh} \in \mathbb{R}^N$. In Eq. (12), the second equality is a direct consequence of $f_d(x, \dot{x})$ being an odd function of $\dot{x}$ (see Appendix E). Comparing Eqs. (4) and (12), it is observed that *the external force vector associated to the motion onto a monophase CNM is also monophase and characterized by a phase lag of $\pi/2$ of each harmonic with respect to the displacement response, regardless of the form of the dissipative forces.*

Therefore, applying a force appropriation procedure, *i.e.* controlling the frequency ω of the external force $f_e(t)$ as well as the shapes $\hat{f}_{eh}$ for $h = 1, 2, \ldots, H$ of its harmonics such that their phases have a phase lag of $\pi/2$ with respect to the corresponding harmonic of the displacement $x(t)$ enables *the conservative nonlinear mode x_{cnm} to be measured, regardless of the dissipative forces.* This conclusion, proven in [33] for the case of a linear damping law $f_d = D\dot{x}$ with a constant damping matrix D, is the basis of experimental nonlinear force appropriation methods, used in a large number of works [34,35,38–40,72,73]. To the knowledge of the authors, the present extension to any arbitrary dissipative force $f_d(x, \dot{x})$ was only suggested previously in a comment of [33], but not addressed in detail as here.

2.6. Imperfect space and frequency dependence for force appropriation

In practice, realizing the exact force appropriation, *i.e.* finding the vectors $\hat{f}_{eh}$ that exactly cancel the harmonics of $f_d(x_{\mathrm{cnm}}, \dot{x}_{\mathrm{cnm}})$ according to Eq. (12), implies two aspects. First, the correct space shape of the vectors $\hat{f}_{eh}$ (the relative value of their components) must be found, such that these vectors mirror the damping space distribution. Secondly, enough harmonics (the number H of Eq. (12)) must be included in the forcing. These two aspects are *a priori* unknown and almost impossible to fulfill in practical experiments, particularly the former. However, if Eq. (12) were perfectly respected, the motion would be on the ith nonlinear mode resonance, *i.e.* very close to the ith invariant manifold of the CNM. As shown in [34,74] using normal form theory, because of the resonant motion, the *space distribution* of the force is not important at first order. This concept can be thought of as the extension of the linear resonance concept to the nonlinear regime: if the modes of a structure are spaced far enough apart in frequency and not too damped, the motion at a given resonance is governed by only one mode, whatever be the space distribution of the forcing. In practice, then, the space distribution of the forcing can be chosen arbitrarily, or, more realistically, according to the apparatus available. In previous works, point forcing has been used successfully in experiments [34,35,35,38,39,41,75,76], as well as piezoelectric forcing [42] or base acceleration forcing, as in the present work and in [40,77,78].

Regarding the second aspect, *i.e* the number of harmonics, it is theoretically possible to synthesize several harmonic components in the force and to control the relative amplitude of the harmonics in order to fulfill the phase lag criterion. However, a single harmonic forcing is often sufficient for force appropriation and used in most cases for the sake of simplicity. It is for this reason that all experimental works on successful nonlinear phase resonance testing in the literature involve only a single harmonic in the forcing (see the above references).

In conclusion, the basic strategy described above (*i.e* with a simple forcing – point forcing or base acceleration forcing, which may be theoretically imperfect – and only one harmonic in the forcing signal) should be sufficient to estimate a given CNM of a structure, so long as the CNM is well-separated from other CNMs and not coupled to some of them because of internal resonances. In other words, the present basic phase resonance strategy will successfully work to measure the backbone curve of the CNM in all locations away from any internal resonances branches, or, more theoretically, if the underlying invariant manifold is two-dimensional.

If internal resonances are of concern, as considered at the end of Section 2.3, the situation is more complex since the response is often not monophase and the dimension of the underlying invariant manifold is more than two-dimensional. As a consequence, measuring internally resonance nonlinear modes with force appropriation must be carefully realized. For a simple 1:1 internal

resonance between companion modes of a structure with symmetries, the coupled elliptic modes are naturally measured with basic phase resonance testing (see [41,42]). In other cases, more than one harmonic in the forcing and a dedicated input force distribution may be necessary, as shown in [79,80] for 1:1 and 1:5 internal resonances, respectively, in clamped–clamped structures. For more complex dynamics such as quasi-periodic or even chaotic responses, phase resonance cannot be applied as explained in the present article since it is restricted to periodic responses.

2.7. The case of non-smooth nonlinearities

Although the present work is restricted to smooth nonlinearities, it is worth considering application of the concepts discussed here to non-smooth nonlinearities. A series of papers [35,76,78,81] explores the use of phase resonance testing to treat the case of structures with strong non-smooth nonlinearities, such as impact and dry friction. In the case of *conservative* non-smooth nonlinearities such as impact without dissipation at the interface, the conclusions of this work may hold: a phase resonance method can be used to measure the conservative backbone curve [76].

The same cannot be said for the case of dry friction. Upon first examination, dry friction forces could be considered to follow the definition of $f_d(\dot{x})$ since they dissipate energy and most models define them as odd functions in $\dot{x}$ [59,82,83]. Following the results of Section 2.5, applying a phase resonance condition to a system for which the only nonlinearities are dry friction would lead to measuring the nonlinear mode of the conservative associated system, which in this case would be purely linear. A straight backbone curve, with constant frequency (equal to the natural frequency of the mode under concern), would be obtained. However, some works [35,78,81,84] show that applying a phase resonance method to such a system leads to a different result: it measures a *damped nonlinear mode*, with a non-straight backbone curve in contrast to the straight backbone curve typical of those systems. This discrepancy can be explained considering that dry friction typically includes both sticking and slipping phases during an oscillation period, the first being purely conservative and the second purely dissipative. As a consequence, dry friction forces are responsible for both *conservative* and *dissipative* nonlinear effects that cannot be separated as in Eq. (1).

3. Numerical estimation of backbone curves and damping with phase resonance

To illustrate the results of Section 2 and validate the theory, in this section a method is presented that solves Eq. (1) *numerically* under the condition of phase resonance. Here, we consider the case of a vertical cantilever beam subjected to gravity in order to establish reference numerical solutions to compare later to the experimental results of Section 4. To this end, the continuation method used in [18,19] based on a combination of the Harmonic Balance Method (HBM) and the Asymptotic Numerical Method (ANM) is slightly modified to compute the periodic solutions of the system in phase resonance.

3.1. Computing the backbone curves with phase resonance

As in [19], we consider a vertical cantilever beam within a gravitational field subjected to a monoharmonic base excitation with motion restricted to the plane. A geometrically exact beam model discretized using Timoshenko finite elements is used to described the motion of the system, written according to [19] as:

$$M\ddot{x} + D\dot{x} + f_c(x) = f_g + f_e(t) \tag{13}$$

where x gathers all the degrees of freedom (the axial displacement, the transverse displacement and the rotation of all the finite element nodes), M is a constant inertia matrix, D is a constant damping matrix, f_c is the internal force vector, which is nonlinear due to the presence of geometrical nonlinearities, f_g is a constant vector due to gravity and $f_e(t)$ is the external force vector.

In the HBM, $x(t)$ is expanded in Fourier series as:

$$x(t) \simeq \hat{x}_0 + \sum_{h=1}^{H} \left[\hat{x}_h^c \cos(h\omega t) + \hat{x}_h^s \sin(h\omega t) \right], \tag{14}$$

where $\hat{x}_0 \in \mathbb{R}^N$, $\hat{x}_h^c \in \mathbb{R}^N$ and $\hat{x}_h^s \in \mathbb{R}^N$ are the Fourier coefficients. Then, introducing Eq. (14) into Eq. (13) and balancing each harmonic, the following algebraic system is obtained:

$$R(X, \omega, \lambda) = 0, \tag{15}$$

with $R \in \mathbb{R}^{2H+1}$, $X^T = [\hat{x}_0^T, \hat{x}_1^{cT}, \dots \hat{x}_H^{cT}, \hat{x}_1^{sT}, \dots \hat{x}_H^{sT}]^T \in \mathbb{R}^{2H+1}$ and $\lambda \in \mathbb{R}$ a bifurcation parameter that is described below. The system (15) has thus $2H + 1$ equations for $2H + 3$ unknowns and an additional phase condition must be added to ensure that the continuation problem be well-posed.

To compute the conservative nonlinear modes of the system, two possibilities are considered here:

- The first (called here method A) is the method described in [18] to solve Eq. (13) in free vibration ($f_e = 0$) with a damping term corresponding to $D\dot{x} = \lambda\dot{x}$, where $\lambda \in \mathbb{R}$ is a fictitious bifurcation parameter used to avoid numerical instabilities [85,86]. In this case, a theoretical periodic solution would naturally lead to a zero value of λ since periodicity is associated with a conservative system. In practice, numerical solutions lead to a very small $\lambda \simeq 0$ because of unavoidable numerical approximations. In this autonomous system, the phase condition can take several forms; the one described in [18] consists in setting to zero the initial velocity of a given component of $\dot{x}$ (*i.e.* $[\dot{x}(0)]_i = 0$, for a given $i \in \{1, \dots, N\}$).
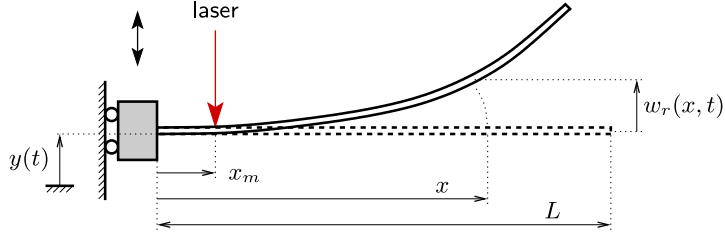
Fig. 1. Sketch of the cantilever beam in prescribed base acceleration $\gamma(t) = \ddot{y}(t)$.
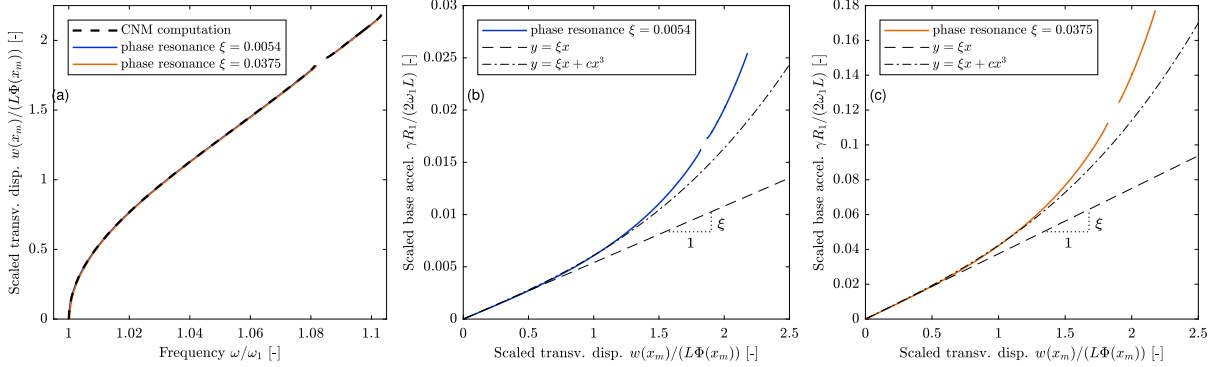

Fig. 2. (a) Backbone curve of mode 1 computed by two numerical strategies: the classical one of [18,19] (black dashed line, method A) and a phase resonance numerical continuation (method B) with $\xi = 0.0054$ (blue solid line) and $\xi = 0.0375$ (orange solid line); (b) base acceleration as a function of the amplitude of beam 1 on the backbone curve computed with method B with $\xi = 0.0054$, and several polynomial fits (c) idem as (b) with $\xi = 0.0375$. The simulation is carried out with mass proportional damping with $\xi \in \{0.0054, 0.0375\}$ as indicated, for a beam of length $L = 380$ mm, width $b = 18.1$ mm and thickness $h = 0.495$ mm (corresponding to experimental beam 1, see Table 1) and with $\alpha = 1.211$ (see Section 5.1). Note that due to the particular scaling of the x- and y-axes, the slope of the linear fit is directly ξ in Figs. (b,c). The first harmonic $w_1(x_m)$ (Eq. (19)) of the transverse displacement at the measurement point x_m is plotted. (For interpretation of the references to color in this figure legend, the reader is referred to the web version of this article.)

- The second (method B), original to the knowledge of the authors, is based on the condition of phase resonance. Inspired by the results of Section 2, the system is forced with a monoharmonic signal $f_e(t) = \lambda f_{e1} \sin \omega t$, with $f_{e1} \in \mathbb{R}^N$ a constant amplitude vector and $\lambda \in \mathbb{R}$ a scalar parameter used to modulate the forcing amplitude. In this case, the phase condition is chosen such that the sine component of the first harmonic of a given component of $x(t)$ is set to zero ($[\hat{x}_{sh}]_i = 0$, for a given $i \in \{1, \ldots, N\}$), thus naturally imposing a $\pi/2$ phase shift between this component and the forcing vector as required for the phase resonance. In the simulations of this work, the selected ith component of $x(t)$ is the transverse displacement at the node located at $x = x_m$ (the location of the sensors, see Section 4.1) and f_{e1} is a uniform vector, chosen to model the forcing due to the base acceleration (see Section 3.2). The damping matrix is specified as mass-proportional, such that $D = 2\omega_1 \xi M$ with ω_1 the first natural frequency and $\xi \in \mathbb{R}$ the damping ratio of the first mode.

3.2. Phase resonance under base acceleration

When a structure is subjected to a base acceleration, its motion *relative* to the motion of the base is described by the classical equations of motion with a uniformly distributed external forcing proportional to the acceleration of the base, as shown in Appendix B. The phase resonance simulation/testing of this work can therefore be applied to a structure subjected to base acceleration, provided the phase lag is enforced between the acceleration of the base $\gamma(t) = \ddot{y}(t)$ and the displacement field $w_r(x, t)$ of the structure *relative* to the base (see Fig. 1).

3.3. Numerical CNMs and damping with phase resonance

Fig. 2(a) combines in one figure the first backbone curve of a cantilever beam computed both with the standard method A (black curve) and with the phase resonance method B of Section 3.1, with, fort the latter, two damping ratio: $\xi = 0.0054$ (blue curve) and $\xi = 0.0375$ (orange curve). The three curves can be seen to overlap perfectly on a very large frequency range up to very large rotation amplitudes, on the order of $180°$ at the tip of the beam. This comparison validates on this example the phase resonance method B for computing conservative nonlinear modes. In particular, for this case, it is not necessary to include a more complicated forcing vector f_{e1} that exactly matches the damping vector $D\dot{x}$ or to add higher harmonics than the first in order to compute the CNM (recall Section 2.6).
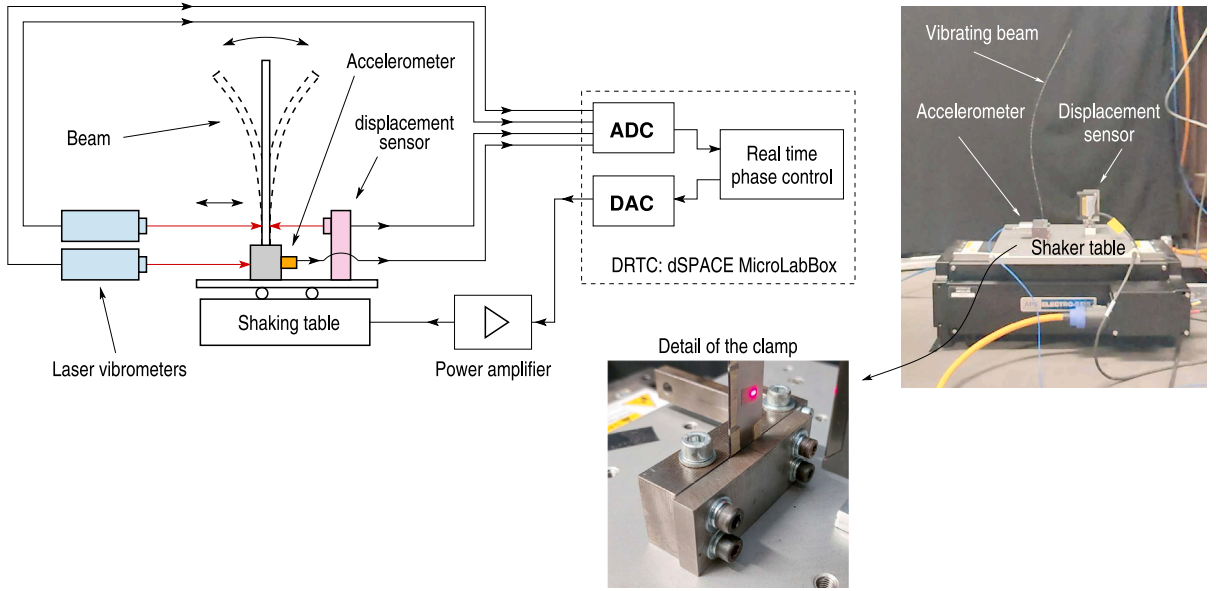
Fig. 3. Experimental setup. The two laser vibrometers are not shown.

In addition to the backbone curves, the amplitude of the first harmonic of the scaled base acceleration is plotted as a function of the scaled transverse beam displacement in Fig. 2(b,c) (refer to Section 4.4 for details on the scaling procedure). For a system containing purely linear damping, the displacement would increase proportional to the acceleration and Fig. 2(b,c) would depict a linear relationship. This is illustrated with the dashed line, the slope of which is proportional to the linear damping factor ξ. It is observed in Fig. 2(b,c) that this linear evolution is valid only at very small amplitudes of motion. At higher amplitudes, the relationship follows a cubic trend (depicted with a dash-dotted curve), eventually turning into even higher orders (quintic, etc.) at extreme amplitudes. This is in agreement with the theory of Appendix A.2 as well as with the findings of Amabili et al. [21,60,87–91], where nonlinear damping models (*e.g.* Kelvin–Voigt in [21]) were used to match experimental frequency response curves for large amplitude vibrations of cantilever beams in a vacuum.

Moreover, it can be seen that the value of the damping factor used for the phase resonance computations (method B) has no influence on the backbone curve (Fig. 2(a)), but changes only the value of the base acceleration necessary to move the beam at resonance: in comparing the y-scales of Figs. 2(b,c), the larger damping of $\xi = 0.0375$ leads in turn to a higher base acceleration in Fig. 2(c), but with an overall trend identical to that of Fig. 2(b).

4. Experimental method for measurement

In this section, the experimental setup and procedure for measurement of the frequency responses and mode shapes of cantilever beams at very large amplitude are described. Unlike in [21,26], where a high speed camera is used to measure both frequency responses and mode shapes, we here rely on a measurement strategy involving two different sensors. The frequency response measurements of this work are carried out using a Phase-Locked Loop (PLL) controller (which, applied to the present highly flexible structures, is an originality of this work) based on the one described in [34] which enables real-time control of the phase between the external applied force and the motion of the structure. By imposing a constant $\pi/2$ phase lag as described in Section 2, the backbone curve of a CNM of the structure is measured. Besides the backbone curves, prescribing a phase sweep in the PLL allows for the whole frequency response to be measured, including its unstable parts. To carry out such measurements, real-time signals are needed, precluding the use of a camera. We relied instead to a displacement sensor or a laser vibrometer, which measure the motion of the beam at a single point in real time. In parallel, the nonlinear mode shape of the structure is extracted from a series of stroboscopic snapshots taken in this case with a camera. The details of these procedures are given in the sections that follow.

4.1. Experimental setup

In each experiment, a beam is fixed to the moving table of a long stroke shaker SPEKTRA APS-113 using a dedicated clamp (the beams are described in Section 5.1 and in Table 1) as shown in Fig. 3. The shaker is powered by an APS-125 power amplifier and provides an acceleration to the base of the cantilever. The control of the experiment is performed using a dSPACE MicroLabBox 1302 digital real-time controller (DRTC). Following the discussion of Section 2.6, a monoharmonic (sinusoidal) signal is selected, generated by the DRTC and fed to the power amplifier to drive the shaker.

As mentioned in Section 3.2, two different measurements are needed: the motion of the shaker table relative to the ground and the motion of the beam relative to the table. A PCB 393B04 piezoelectric accelerometer capable of measuring low frequencies (down to 0.06 Hz) is screwed to the shaker table to measure its acceleration and serve as a reference for all phase measurements. Two sets of sensors are then introduced to measure the displacement of the beam. The first, a Keyence IL-065 laser displacement sensor, is likewise screwed onto the shaker table and measures the displacement of one point of the beam *relative* to the shaker table. This point is chosen close to the clamping point of the beam, at a distance $x = x_m = 18$ mm from the clamp (this point is discussed more below). The second set of sensors is made up of two Polytec laser vibrometers (a PSV-400 and a OFV-505). The first of these is directed at the shaker table while the second one is directed at the same location as the displacement sensor, $x = x_m = 18$ mm from the clamp, such that the velocity of the vibrating beam relative to the table is obtained by subtracting the two vibrometer signals. This subtraction is carried out by the DRTC. Two slightly different velocity decoders are used in the two OFV-5000 vibrometer controllers used for the laser vibrometers (a VD-09 for the first vibrometer and either a VD-04 or a VD-08 for the second).

In theory, the choice of whether to use laser vibrometers or displacement sensors to capture the motion of the beam is open as the three quantities are related and thus should give equivalent measurements. However, in practice, one of the sets of sensors was preferred depending on the frequency range of the targeted mode. When the two laser vibrometers are used, a slight delay is observed at very low frequencies (likely due to the different velocity decoders), leading to an error in the measurement of the beam *relative* to the shaker table. Although this error may be corrected digitally in the DRTC by shifting one signal by a few time samples, the displacement sensor is nevertheless preferred here for (low frequency, see Table 2) measurement of the mode 1 frequency responses. By contrast, the displacement sensor is observed to introduce a constant delay whose influence increases as a function of the frequency. While the delay is found to be negligible on the mode 1 frequency response measurements, this is not the case for modes 2 and 3. For these reasons, the measurements of Section 5 related to mode 1 are taken with the displacement sensor, whereas the set of vibrometers is used for the measurements related to modes 2 and 3.

In each case, the motion of the beam is measured at $x = x_m = 18$ mm, very close to the clamp of the beam in order to avoid measuring too large of displacements (see Fig. 1). The measured displacements must remain in the measurement range of the laser displacement/velocity sensors, but selecting this location furthermore allows for measurement of the Lagrangian motion of a given point of the beam, *i.e.* at a location fixed with respect to the deformed beam. Since the lasers are fixed in an Eulerian reference frame, the exact location of the lasers on the beam shifts slightly during the motion. At $x_m = 18$ mm, this shift is only on the order of 0.5 mm, an uncertainty depicted by the blue regions in Figs. 9–11.

The four sensors (the two vibrometers, the accelerometer and the displacement sensor) are connected to the input of the dSPACE I/O board, with the input of the power amplifier connected to the output of the dSPACE I/O board. The real-time control is based on a Matlab/Simulink schematic, described in [34] and addressed in the following section.

4.2. Frequency response & backbone curve measurements

The DRTC creates a sine signal to drive the shaker table, such that the acceleration of the shaker table can be written:

$$\gamma(t) = \gamma_e \cos \omega t, \tag{16}$$

where ω is the angular frequency of the signal and γ_e is its amplitude. If $w_r(x,t)$ is used to denote the resulting transverse displacement of the beam relative to the shaker table at point x (see Fig. 1), assuming it periodic, the signal measured by the displacement sensor at $x = x_m$ can be written:

$$w_m(t) = w_r(x_m, t) = w_{m0} + \sum_{h=1}^{+\infty} w_{mh} \cos(h\omega t + \varphi_h), \tag{17}$$

where (w_{mh}, φ_h) are the hth harmonic amplitude and phase of the signal. Then, the velocity signal measured by the difference of the two vibrometer signals is written:

$$v_m(t) = \sum_{h=1}^{+\infty} v_{mh} \cos(h\omega t + \psi_h), \tag{18}$$

with $v_{mh} = h\omega w_{mh}$ and $\psi_h = \varphi_h + \pi/2$.

The PLL controls the frequency ω such that the phase lag φ_1 (ψ_1) of the first harmonic of the displacement (velocity) signal with respect to the acceleration signal is as close as possible to a certain prescribed value φ_p. In the present work, the PLL algorithm is based on the work of Denis et al. [34]. However, the main discrepancy with [34] is that the frequency range of the measurements here is notably smaller (on the order of $2 - 4$ Hz, see Table 2) than the frequency range presented in [34]. Because of this, the demodulation algorithm of the PLL must be slightly modified in order to estimate the amplitude and phase of the first harmonic of the signals. In [34], a standard synchronous detector is used: the signal to be demodulated at frequency ω is multiplied by reference signals $\sin \omega t$ and $\cos \omega t$ and the result is low-pass filtered. To minimize any errors, a steady state must be reached and several periods $T = 2\pi/\omega$ must be used in the procedure, a process which in this case is too lengthy due to the long period of the signals (several seconds) and the low damping which induces long transients. Instead, since the precise frequency ω of the signals is known (prescribed by the controller), the low-pass filter is replaced with a computation of the average of the signals over a single period T, measured with precision because of the high sampling frequency of the DRTC (10 kHz). Aside from these considerations, the interested reader is referred to [34] for the details regarding the PLL.
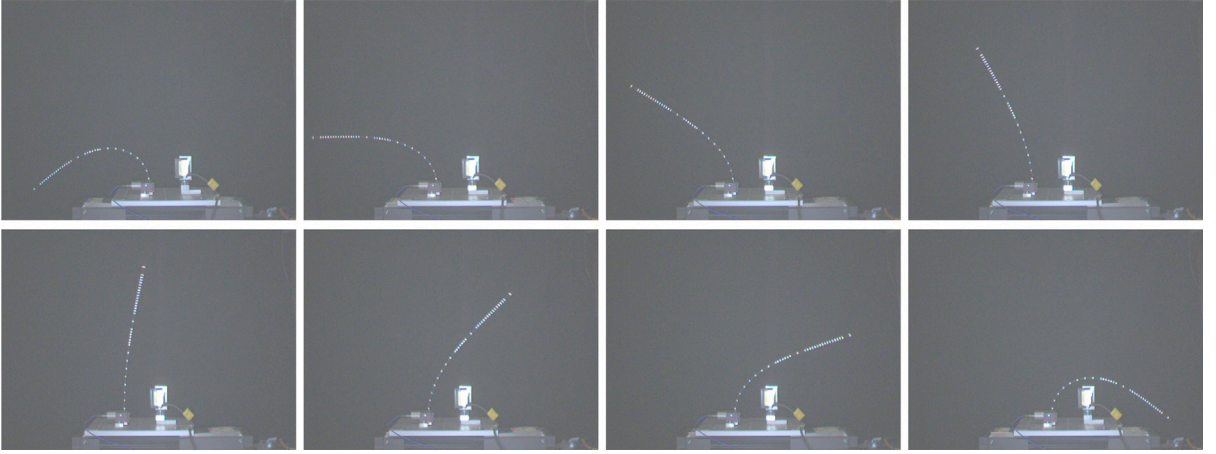
Fig. 4. Eight snapshots of the motion of the cantilever beam excited by base acceleration on its first nonlinear mode over half a period.
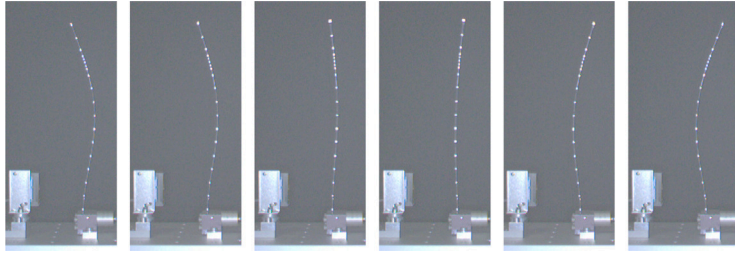

Fig. 5. Six snapshots of the motion of the cantilever beam excited by base acceleration on its second nonlinear mode over half a period.

To measure the backbone curve of a CNM, the phase lag of the beam displacement with respect to the forcing is fixed at $\pi/2$ as explained in Section 2. In the experiments, since the force is proportional to the shaker table acceleration $\gamma(t)$ (see Section 3.2), the backbone curve of a given CNM can be directly measured by prescribing $\varphi_1 = -\pi/2$ in the case of the displacement sensor (or $\psi_1 = 0$ in the case of the vibrometers) and slowly increasing the value of the acceleration amplitude γ_e.

Conversely, to measure a given nonlinear frequency response, the forcing amplitude γ_e is kept constant and a phase sweep of φ_1 is prescribed in $[0, -\pi]$, around $-\pi/2$ (or of ψ_1 in $[-\pi/2, -\pi/2]$). This is due to the main property of the PLL being its capacity (due to its closed loop) to lock onto periodic solutions of the system in open loop (*i.e.* as if vibrating without the PLL), regardless of the stability of the solutions, by stabilizing any which are unstable [34]. Moreover, since the frequency responses around a given resonance have the same topology as that of a simple Duffing oscillator, the phase variation is monotonous around the phase resonance ($\varphi_1 \simeq -\pi/2$ and $\psi_1 \simeq 0$) and the phase sweep enables continuous measurement of the entire frequency response, even in the presence of unstable branches. Note also that, in this scenario, the forcing amplitude γ_e is governed by closed-loop control and makes use of the amplitude measurement obtained by the synchronous detection.

Examples of measured backbone curves and nonlinear frequency responses are given in Figs. 9–11, with some associated phase differences ϕ_1 and ψ_1 in Fig. 12.

4.3. Tracking of the nonlinear mode shapes

In addition to the frequency responses and backbone curves measured by the PLL, the nonlinear mode shapes, *i.e* the motion of the system onto a CNM at a given amplitude, are key in characterizing the nonlinear behavior as the vibration amplitude increases. One possibility for mapping the deformed shape of periodic vibrations is via rapid motion capture using a high speed camera, as done in [21,26]. Another possibility, and the one chosen for this work, is to create a stroboscopic effect over several periods of motion. This is possible with more standard cameras as long as the capture rate can be prescribed.

For a periodic signal of period $T = 1/f$ where f is the frequency, a stroboscopic effect can be created by imposing a periodic capture rate on a recording device equal to n periods of motion plus a small time delay $nT + \Delta t$ where $\Delta t \ll T$. Then, the difference between the deformed shape in one image and the next is equivalent to having captured it at time t_1 and $t_2 = t_1 + \Delta t$ despite the slower overall capture rate. Examples of the types of images captured to track the deformed shape are shown for the first three modes in Figs. 4–6.

A Basler acA640-90uc camera (maximum frame rate 100 fps, sensor size 658×492 pixels) is used together with the Basler video recording software [92] to record the motion. Reflective tape is placed at several locations along the beam length to reconstruct the
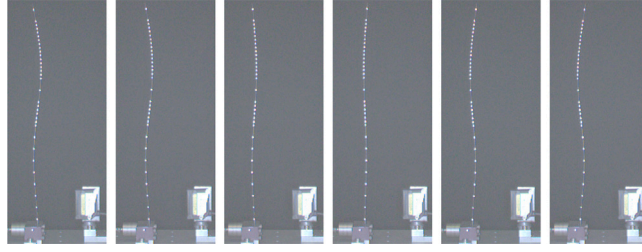
Fig. 6. Seven snapshots of the motion of the cantilever beam excited by base acceleration on its third nonlinear mode over half a period.
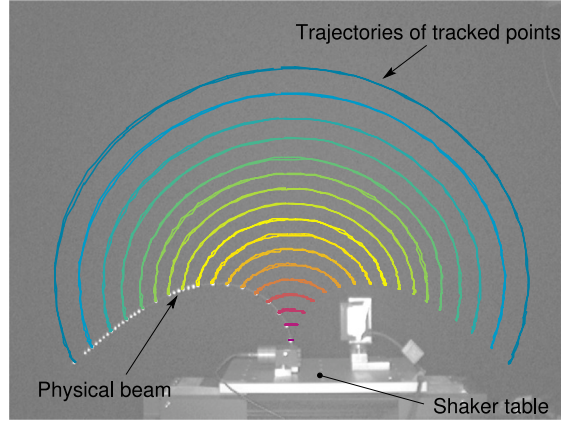

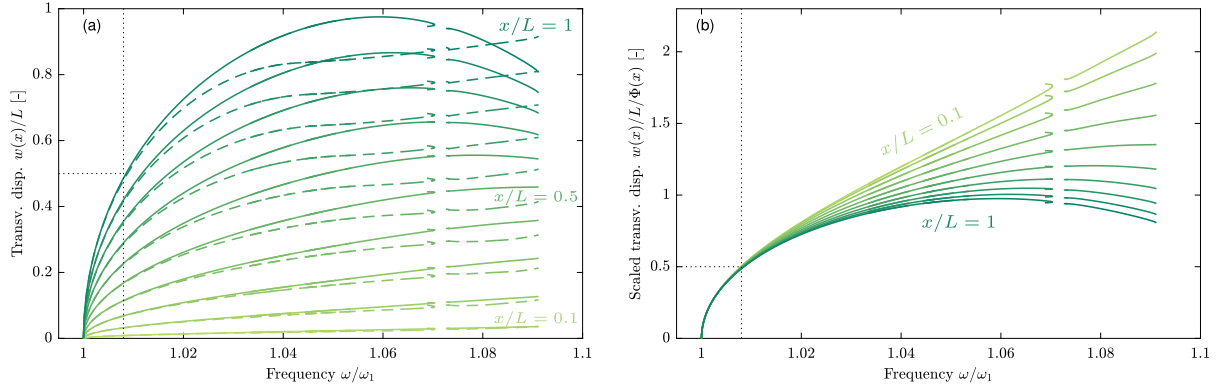**Fig. 7.** First nonlinear mode trajectories of the cantilever beam overlaid onto the first snapshot of Fig. 4.

Fig. 8. (a) Evolution of the backbone curve of mode 1 as a function of the position x on the beam, for $x/L \in \{0.1, 0.2, \ldots, 0.9, 1\}$ (light to dark green when x increases). The first harmonic $w_1(x)/L$ of the transverse displacement is shown in solid line and the maximum $\max_{t \in [0,T]} w(x,t)$ over one period $T = 2\pi/\omega$ of oscillation is shown in dashed lines. (b) Same plot where the first harmonic $w_1(x)/L/\Phi_1(x)$ of the transverse displacement is shown scaled by the linear deformed shape $\Phi_1(x)$. A beam of length $L = 380$ mm, width $b = 18.1$ mm, thickness $h = 0.495$ mm and gravity parameter $\alpha = 1$ (slightly lower than for experimental beam 1) is considered. (For interpretation of the references to color in this figure legend, the reader is referred to the web version of this article.)

deformed shape of the beam with appropriate spatial discretization, as shown in Figs. 4–6. In shining light onto the reflective tape (in dim surroundings), distinct illuminated points appear in each of the stroboscopic images.

The DLTdv digitizing tool [93], which interfaces with MATLAB, is then used for multi-point tracking between the images. This software allows the illuminated points to be tracked automatically through the series of images and returns their trajectories in space. An example of the tracked trajectories of the first nonlinear mode overlaid onto a sample image is shown in Fig. 7.

4.4. Scaling of the measured quantities

Due to the presence of geometrical nonlinearities in the very large deformations that are targeted in this work, the shape of the backbone curve of a given nonlinear mode depends on the location x along the beam where it has been measured, a dependence

that is potentially complex. To illustrate this, consider the motion on the kth CNM, where the beam's motion relative to the base is periodic and monophase, written as:

$$w_{\mathrm{r}}(x,t) = w_0(x) + \sum_{h=1}^{+\infty} w_h(x)\cos(h\omega t + \varphi_h). \tag{19}$$

If the nonlinear mode shape were independent of the amplitude of the motion, Eq. (19) would condense into:

$$w_{\mathrm{r}}(x,t) \simeq a\Phi_k(x)\cos(\omega t + \varphi_1), \tag{20}$$

with $\Phi_k(x)$ the kth "linear" mode shape, such that $w_1(x) = a\Phi_k(x)$ and all the other harmonics in Eq. (19) are zero ($w_h(x) = 0$ for all $h \neq 1$).

If the nonlinear mode shape were independent of the amplitude (Eq. (20)), simply plotting the backbone curve with the first harmonic $w_{\mathrm{m}1}$ of $w_{\mathrm{m}}(t) = w_{\mathrm{r}}(x_{\mathrm{m}},t)$ as a function of ω would be sufficient to recover the backbone for *any* value of x with a simple scaling, namely $w_1(x) = a\Phi_k(x) = w_{\mathrm{m}1}\Phi_k(x)/\Phi_k(x_{\mathrm{m}})$. In particular, it would be possible to recover the backbone curve of the tip of the beam by plotting $w_1(L) = w_{\mathrm{m}1}\Phi_k(L)/\Phi_k(x_{\mathrm{m}}) = w_{\mathrm{m}1}/\Phi_k(x_{\mathrm{m}})$, with $\Phi_k(x)$ normalized such that $\Phi_k(L) = 1$, with L the length of the beam.

However, the present case of a beam in very large displacement has a nonlinear mode shape that depends on the amplitude, as seen for instance in Fig. 13, such that the backbone curve plotted for $w_{\mathrm{m}1}$ is different than the one plotted for $w_1(x)$ for $x \neq x_{\mathrm{m}}$. This is illustrated in Fig. 8(a), where the effect of the large amplitude of motion is clear above $w(L) \simeq 0.5L$ (see the black dotted line). Below the limit $w(L) \simeq 0.5L$, all the scaled backbones plotted at different points x collapse into a single one in Fig. 8(b), indicating that the deformed shape is exactly $\Phi_1(x)$. Above this limit, however, the backbones diverge because of the large amplitude of the motion. A similar effect is also observed in Fig. 8(a) where the effect of the higher harmonics separates the backbones plotted as maximum amplitudes over one period (dashed lines) from those depicting only the first harmonic (solid lines).

For those reasons, to give more generality into the frequency responses and backbone curves measured at $x = x_{\mathrm{m}}$, we adopt the same scaling as if the mode shapes were independent of the amplitude: in what follows, $w_{\mathrm{m}1}/L/\Phi_k(x_{\mathrm{m}})$ is plotted instead of $w_{\mathrm{m}1}/L$, to give an idea of the related tip displacement. Note that the displacement is also scaled by L, as introduced in Eqs. (23). Consequently, having $w_{\mathrm{m}1}/L/\Phi_k(x_{\mathrm{m}}) = 1$ would indicate a tip displacement equal to the length of the beam *if the mode shape were independent of the amplitude*. In the present case, however, the scaling gives only *qualitatively* the order of magnitude of the tip displacement. The analytical expression of $\Phi_k(x)$ for a cantilever beam is used in this scaling (see [94]).

Regarding the base acceleration, instead of directly using the amplitude γ_e [m/s^2] of the base acceleration, it is scaled as $\bar{\gamma}_e = R_k\gamma_e/(2\omega_k^2 L)$ for the frequency response of mode k, explained in Appendix B. For a linear beam model with linear viscous damping of modal ratio ξ_k, the amplitude of the first harmonic of the transverse displacement at the tip $x = L$ is:

$$\frac{w_1(L)}{L} = \bar{w}_1(x) = \frac{\bar{\gamma}_E}{\xi_k}, \tag{21}$$

such that the value of the damping ratio ξ_k is easily read by the slope of the tangent at the origin in Figs. 2 and 17.

5. Results for the first three nonlinear modes of a vertical cantilever

This section is dedicated to measurement and analysis of the CNMs with phase resonance testing and comparison to the finite element geometrically exact numerical model of [18,19], with additional insight into the damping of the system. As explained in the introduction, the aims can be summarized as: (1) investigate the nonlinear dynamics of cantilever beams at very large amplitude, (2) validate the geometrically exact beam model, (3) validate the phase resonance concept introduced in Section 2 and (4) use the phase resonance concept to estimate a damping law up to very large amplitudes of motion.

5.1. Beams under study

Three different beams are used in the experiments, referred to as beams 1, 2 and 3. The beams used are stainless steel rulers whose length L greatly exceeds the width b and thickness h of the cross section ($h \ll L$ and $b \ll L$). All beams have the same thickness. Beams 1 and 2 are of the same length L, but have different widths b, and beam 3 is shorter and has a width smaller than the previous two. The geometry and material properties of the beam specimens are summarized in Table 1 and their measured natural frequencies (first three modes) in Table 2. The measured mass and dimensions of each beam are used to determine the density ρ of each specimen. Slight differences in the thickness h were measured across the length of the beam represented by the ±0.005 mm uncertainty in h, leading to a range of values for ρ. Classical tensile tests are used to determine the ratio of the Young's modulus E to ρ as shown in Appendix G, and the resulting E/ρ ratio of each beam is used to compute the E of each material.

In [19], it is shown that the equations of motion of the geometrically exact beam model depend only on three dimensionless parameters:

$$\eta = \frac{1}{12}\frac{h^2}{L^2}, \quad \mu = \frac{2(1+\nu)\eta}{k}, \quad \alpha = \frac{\rho g L}{E\eta}, \tag{22}$$

with k the shear correction factor, ν the Poisson ratio and ρ the gravity acceleration, when the position x, transverse displacement w and the frequency ω are normalized according to:

$$\bar{x} = \frac{x}{L}, \quad \bar{w} = \frac{w}{L}, \quad \bar{\omega} = \omega L^2\sqrt{\frac{\rho A}{EI}}. \tag{23}$$

Table 1
Characteristics of the three tested beams.

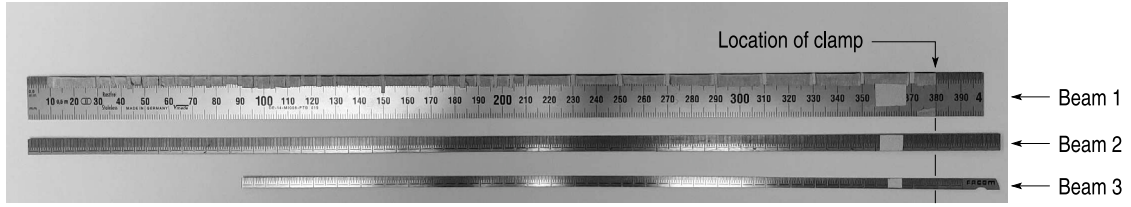|			Beam 1	Beam 2	Beam 3
Brand			VMADE	FACOM	FACOM
Length	L	[mm]	380	380	290
Width	b	[mm]	18.1	6.79	4.43
Thickness	h	[mm]	0.49 – 0.5	0.49 – 0.5	0.49 – 0.5
Slenderness	η	$[10^{-7}]$	1.39 – 1.44	1.39 – 1.44	2.38 – 2.48
	h/L	[–]	$1.30 \cdot 10^{-3}$	$1.30 \cdot 10^{-3}$	$1.70 \cdot 10^{-3}$
	b/L	[–]	$4.76 \cdot 10^{-2}$	$1.79 \cdot 10^{-2}$	$1.53 \cdot 10^{-2}$
	b/h	[–]	36.3	13.7	8.95
Young's modulus/density	E/ρ	$[\mathrm{MPa} \cdot \mathrm{m}^3/\mathrm{kg}]$	21.77	24.37	24.37
Density	ρ	$[\mathrm{kg/m}^3]$	7988 – 7828	7882 – 7724	7882 – 7724
Young's modulus	E	[GPa]	173.9 – 170.4	192.1 – 188.3	192.1 – 188.3
Gravity parameter	α	[–]	1.236 - 1.187	1.104 – 1.06	0.491 – 0.471

Table 2
Experimental natural frequencies (in Hz) of the three tested beams for the first three modes.

	Beam 1	Beam 2	Beam 3
$\omega_1/(2\pi)$	2.47	2.18	4.04
$\omega_2/(2\pi)$	16.62	14.85	26.45
$\omega_3/(2\pi)$	46.92	41.92	74.48

These dimensionless parameters η, α and μ represent, respectively, a slenderness parameter, a gravity parameter and a shear parameter (tied to the Timoshenko kinematics). Neglecting the shear parameter μ (it is shown in [19] that it has virtually no influence since the beams are slender), the values of η and α for all three beams are shown in Table 1.

In [19], it is shown that the slenderness parameter η has very little effect on the first three CNMs as long as it remains small ($\eta \leq 10^{-6}$). The value of the slenderness parameter η for each beam falls in the range $\eta = 1 \cdot 10^{-7}$ and $2.5 \cdot 10^{-7}$, indicating extreme slenderness. The ruler beam specimens of these experiments are therefore very representative of the slender structures that are the focus of our work.

By contrast, it is shown in [19] that the effect of gravity, represented by the dimensionless parameter α, has a significant hardening effect on the backbone curves of the first nonlinear mode of a standing cantilever. On the second and third nonlinear modes, however, the influence of α is almost negligible. The values of α for each of the beams are shown in Table 1 and range between 0.471 and 1.236. Without incorporating the effect of gravity into the model (*i.e.* for $\alpha = 0$), a strong discrepancy between the experimental and numerical backbone curves of the first nonlinear mode is found. This is depicted in Fig. 10(a) where the effect of gravity is the strongest: the theoretical backbone curve without the effect of gravity diverges immediately from the theoretical backbone curve including the effect of gravity, an effect already noticed in [26].

In addition, for appropriate comparison between theory and experiments, two uncertainties mentioned previously must be taken into account: a first uncertainty tied to the measurement position x_m, depicted with a blue shaded area on the curves, and the uncertainty on h, depicted with a pink shaded area. In the model, the variation on x_m is computed by measuring the displacement of two different nodes of the finite element mesh, located at the extreme values of x_m. The variation of h, however, affects only the value of the gravity parameter α, since all simulations of this work are scaled (without the effect of gravity, the effect of h would be negligible in theory since it affects only the value of η).

5.2. Backbone curves

We now proceed to comparison of the experimentally-measured backbone curves to those of the numerical model. In this section, the first three nonlinear modes of beams 1, 2 and 3 are studied in Figs. 9 and 11. The numerical simulations are carried out using beams with the same properties as beams 1, 2 and 3, discretized into 23 finite elements (24 nodes; 21 equally spaced nodes plus three additional nodes located at $x_\mathrm{m} = 18 \pm 0.5$ mm. In Figs. 9 and 11, the backbone curves representing the first harmonic (H1) of the scaled transverse displacement $w(x_\mathrm{m})/L/\Phi_k(x_\mathrm{m})$, measured at the point x_m along the length of the beam, are plotted (see Section 4.4 for details on this scaling). Fig. 10 is a direct copy of Fig. 9, but with a zoom onto only the backbone curves.
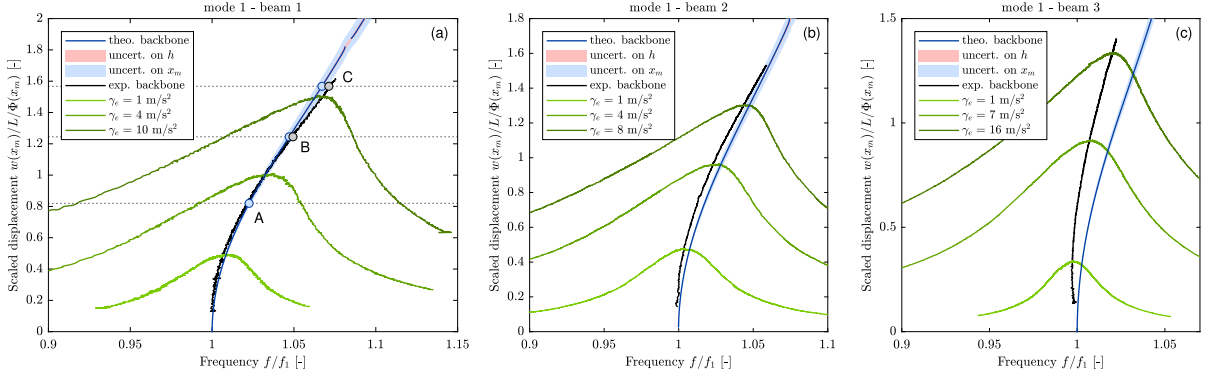
Fig. 9. Experimental nonlinear frequency responses, for several base accelerations, and backbone curves (displacement sensor) of mode 1 compared to the theoretical backbone curve. The light blue and pink shaded area correspond to the measurement uncertainty of the theoretical backbone curve due to, respectively, the beam thickness h and the measurement position $x_{\rm m}$ (a): beam 1; (b): beam 2; (b): beam 3. (For interpretation of the references to color in this figure legend, the reader is referred to the web version of this article.)
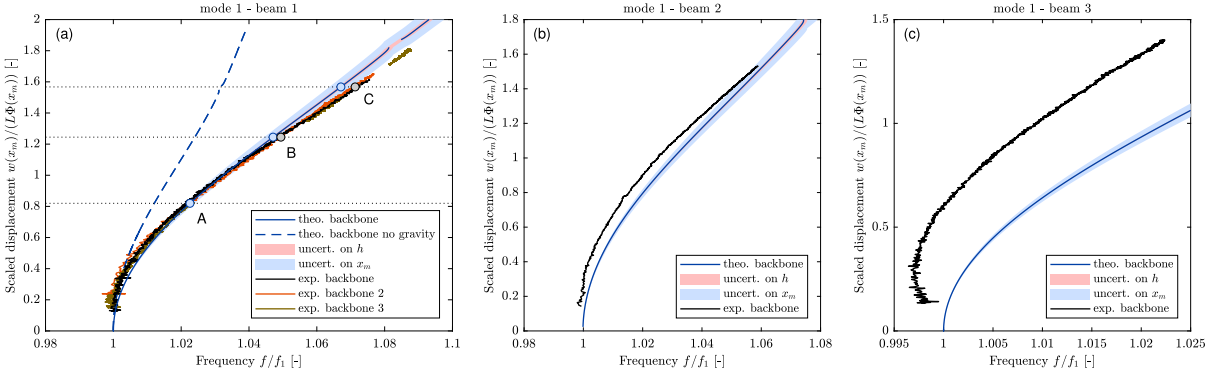

Fig. 10. Experimental backbone curves (displacement sensor) of mode 1 compared to the theoretical one. The light blue and pink shaded area correspond to the measurement uncertainty of the theoretical backbone curve due to, respectively, the beam thickness h and the measurement position $x_{\rm m}$. (a): beam 1; (b): beam 2; (c): beam 3. (For interpretation of the references to color in this figure legend, the reader is referred to the web version of this article.)

In addition to the backbone curves, experimental nonlinear frequency responses are shown for three amplitudes of the base acceleration in these figures. Since an appropriate nonlinear damping model is not as of yet implemented in the finite element code, a significant mismatch would be observed between experimental and numerical frequency responses. More discussion on the topic is postponed to Section 5.4, which addresses the subject of damping along with additional topics. For these reasons, the experimental nonlinear frequency responses are not compared to numerical simulations here.

Nonlinear mode 1. Beginning with the first nonlinear mode of the cantilever, very good agreement is found between the experimental and numerical backbone curves for the two longer beams, beam 1 in Figs. 9(a) and 10(a) and beam 2 in Figs. 9(b) and 10(b). In the zoom of the backbone curves in Fig. 10, it can be seen that the experimental backbone curves of beams 1 and 2 remain within or very close to the uncertainty range of the numerical backbone (uncertainty on h and $x_{\rm m}$, see Section 4.1 and Section 5.1), even up to very large amplitudes (the amplitude of the beam is more clearly visible in the snapshots of the deformed shape, see *e.g.* Fig. 13 for the first nonlinear mode of beam 1). The known hardening trend of the first nonlinear mode of the cantilever beam is recovered for all three beams by the experimental measurements. However, the experimental backbone curve of the shorter beam 3, in Figs. 9(c) and 10(c), presents a shift in frequency from the numerical backbone because of a slight softening effect at low amplitude. This is likely attributed to an imperfect clamp, the effect of which is larger on beams with smaller width, since this distortion also seems to appear on a smaller scale for the experimental backbone of beam 2. It can also be attributed to a non-zero curvature at rest (even if it was observed negligible), as a curvature effect can add softening behavior [95].

Several observations can be drawn from these results. The strong effect of gravity on the first nonlinear mode documented in [19] is recovered in Fig. 10(a), where the backbone curve corresponding to the no-gravity condition departs significantly from the backbone curves including gravity. In addition, since the effect of the gravity parameter α decreases with the index of the beam, it is observed by comparing Figs. 10(a,b,c) that the backbone curve of beam 1 is more hardening than that of beam 2, which is likewise more hardening than that of beam 3 (recall that, with the scaled axes, the backbone curves of the three beams are fully comparable). Fig. 10(a) furthermore demonstrates the repeatability of the experiments. Two additional experimental backbone
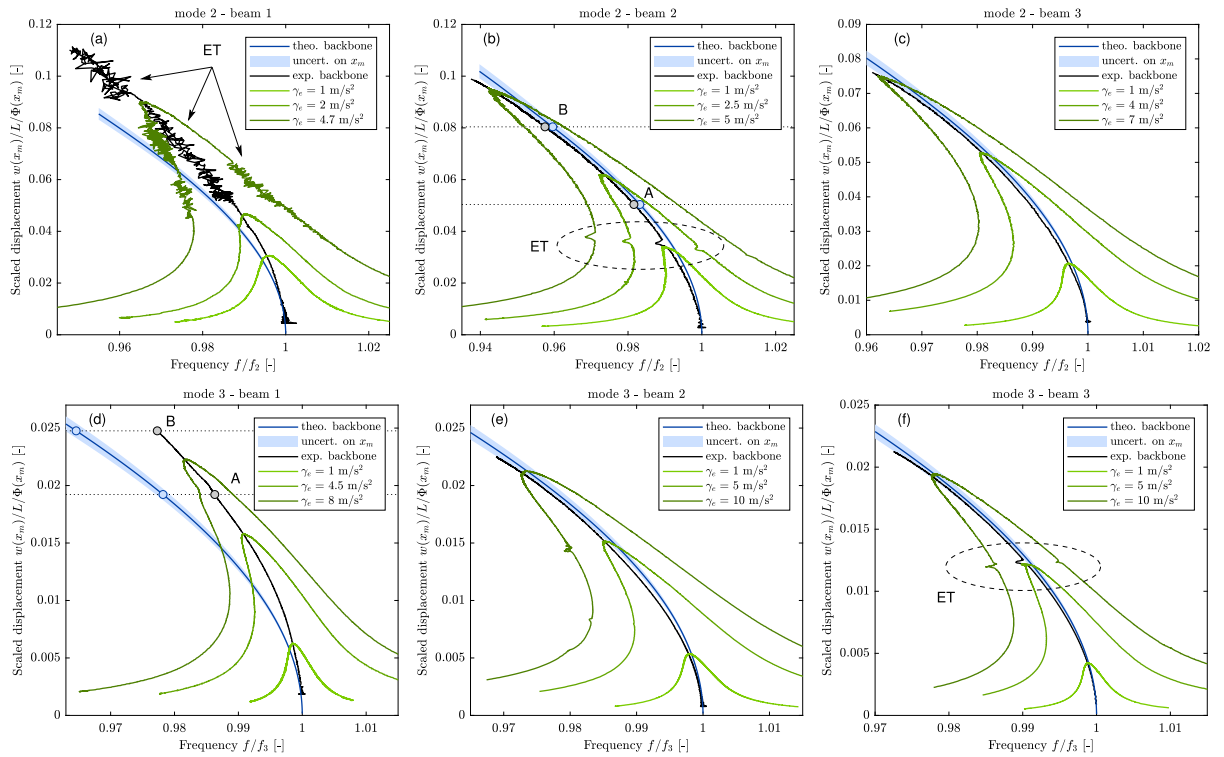
Fig. 11. Experimental nonlinear frequency responses, for several base acceleration, and backbone curves (laser vibrometer) of mode 2 and 3 compared to the theoretical backbone curve. The light blue shaded area correspond to the measurement uncertainty of the theoretical backbone curve due to the measurement position x_m. (a): mode 2, beam 1; (b): mode 2, beam 2; (c): mode 2, beam 3; (d): mode 3, beam 1; (e): mode 3, beam 2; (f): mode 3, beam 3. "ET" means "Energy transfer" and refer to a quasi-periodic regime due to a transfer of energy to mode 1. (For interpretation of the references to color in this figure legend, the reader is referred to the web version of this article.)
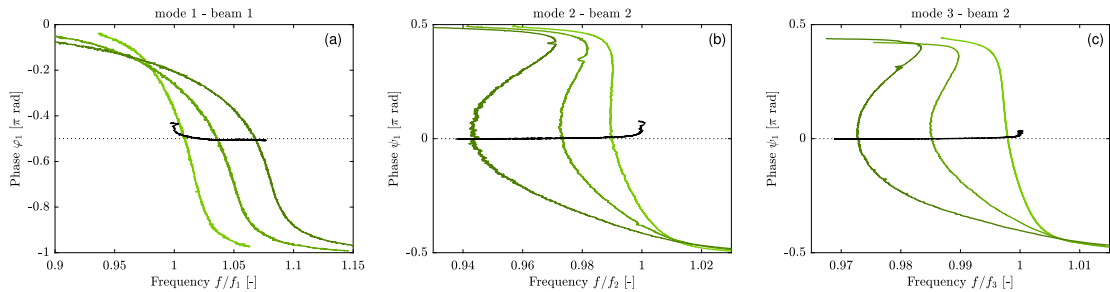

Fig. 12. Phase difference of the first harmonic of beam motion with respect to the acceleration signal. (a) phase φ_1 of signal $w_m(t)$ from displacement sensor for mode 1, corresponding to Fig. 9(a); (b) phase ψ_1 of signal $v_m(t)$ from vibrometers, for mode 2, corresponding to Fig. 11(b); (c) phase ψ_1 of signal $v_m(t)$ from vibrometers, for mode 3, corresponding to Fig. 11(e).

curves (different tests using the same beam) are added in orange and brown to the experimental backbone curve of Fig. 9(a) (in black). The three experimental curves are in excellent agreement, indicating that the experimental procedure of Section 4 is robust and repeatable.

Nonlinear modes 2 and 3. The second and third nonlinear modes of beams 1, 2 and 3 are summarized in Fig. 11, measured following the same procedure as for the first nonlinear mode. The softening trend of both nonlinear modes of a cantilever beam is again recovered experimentally for all three beam specimens. However, unlike the first nonlinear mode, a good agreement between the numerical and experimental backbone curves is found only for the two thinner beams, beam 2 in Figs. 11(b,e) and beam 3 in Figs. 11(c,f). The experimental backbone curves of these two beams remain within or very close to the uncertainty range of the numerical backbone. By contrast, the experimental backbone curves of beam 1 in Figs. 11(a,d) lie far outside the uncertainty window of the numerical backbones and, moreover, are significantly more hardening compared to even beam 2, which has the same slenderness parameter η as beam 1. Since the gravity parameter α has a negligible effect on the second and third nonlinear
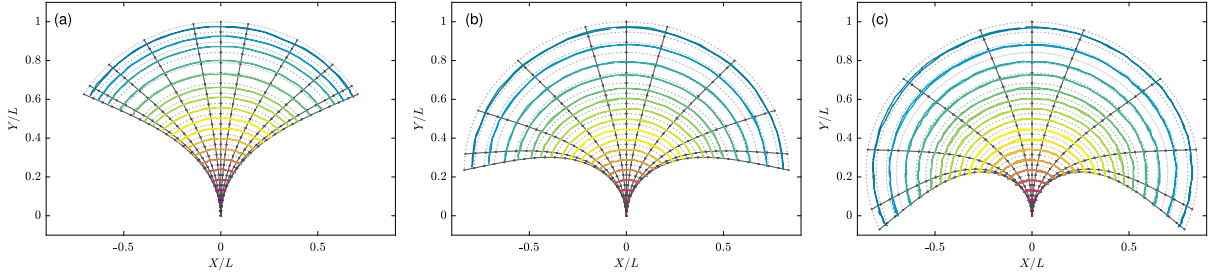
Fig. 13. Deformed shape of the first nonlinear mode of beam 1 for several base accelerations. (a): point A of Figs. 9(a) and 10(a); (b): point B; (c): point C. Equal scale on X and Y axes.

mode [19], the theoretical backbone curves of beams 1, 2 and 3 in Figs. 11(a–f) are near identical. The experimental backbone curves, however, are different, indicating that another effect is influencing the experimental response.

Analyzing the geometry of the beams, these discrepancies could be attributed to a plate/ribbon effect. If the beams are slender in the direction of motion ($h/L \in [1.3, 1.7] \cdot 10^{-3}$), they are less slender in the other directions, especially for beam 1 for which $b/h = 36.3$ and $b/L = 4.76 \cdot 10^{-2}$. In this case, the geometry resembles that of an elastic strip, with $L \gg b \gg h$. This kind of structure, between a slender beam and a thin plate, is associated with so-called plate or ribbon effects. The geometrically exact beam theory of [18,19] neglects the *stresses* in the width direction, leading to a bending stiffness equal to EI (Eq. (A.4)). If a plate model in bending is considered, the *strains* in the width direction are zero and the bending stiffness is larger, equal to $EI/(1 - v^2)$, with v the Poisson's ratio. This latter case is often used in the literature for modeling strip-like beams for which $b \gg h$ [96, §8.11], even if the anticlastic curvature of the cross section of the beam is neglected in this case [55]. In parallel, a so-called ribbon model has been developed [55,97] to take into account the nonlinear static behavior of large-width beams subjected to large amplitude (non-linear) bending (and twisting), including deformations of the cross section in an anticlastic shape. The model introduces a dimensionless curvature parameter $\bar{\kappa} = \kappa b^2/h = (\kappa L)(b/L)/(h/b)$ to scale the ribbon effect, a parameter which includes both the effects of (1) the geometry ($\bar{\kappa}$ increases with b) and (2) some geometrical nonlinearities, since it depends on the bending curvature κ. The model predicts that the bending stiffness of the strip increases as a function of the bending curvature κ and thus as a function of the transverse deflection, thereby predicting a hardening nonlinear effect. At the limit of a small curvature κ and beam width, $\bar{\kappa} \ll 1$, the "beam" bending stiffness EI is recovered; conversely, if $\bar{\kappa} \gg 1$, the bending stiffness tends to $EI/(1 - v^2)$ when κ increases. The present case of nonlinear modes of a cantilever beam is not directly addressed by these works, which do not consider inertia and dynamics, since they are restricted to statics. However, they show qualitatively that the larger $\bar{\kappa}$ is, the larger the stiffness, suggesting that strips (with $b \gg h$) are probably more hardening than the corresponding beam of same dimensions but with $b \simeq h$. Recall that, in the geometrically exact beam model, the linear and nonlinear dynamics are independent of b. This trend, then, can describe the behavior observed on the second and third mode backbone curves of beam 1 in Figs. 11(a,d), where the experimental backbones are less softening than their theoretical counterparts. A similar effect was also noticed with numerical simulations in [10, Appendix C]. Quantitative values of $\bar{\kappa}$ in the experiments are tabulated in Appendix H.

Another interesting effect is locally observed on the frequency responses of modes 2 and 3 (denoted ET in Figs. 11(a,b,f)). This effect is due to an Energy Transfer to mode 1, essentially representative of the high frequency oscillations of mode 2 or 3 modulated by very low oscillations on mode 1. The ET effect leads to a quasi-periodic regime of vibration that cannot be stabilized by the PLL, itself intrinsically dedicated to periodic oscillations. This effect is observed at its strongest on the frequency response of mode 2 of beam 1 (Figs. 11(a)), and is well-documented in the literature where it is described as a transfer of energy between widely spaced modes [2,24,25,98].

5.3. Nonlinear mode shapes

In addition to the backbone curves of the previous section, we compare the deformed shape of the cantilever on its first three nonlinear modes to the experimental deformed shape tracked as described in Section 4.3. Numerically, the deformed shape of the beam is reconstructed directly for all degrees of freedom from the response x_{cnm} at a certain point along the backbone curve (vibrating at a certain amplitude and frequency). The displaced beam is then traced for a number of snapshots (here, 10) over one half period of the motion, with the snapshots of the beam and the trajectory of each of the beam's nodes collected together in one figure. The point along the numerical backbone for which all the deformed shapes are drawn is selected at the same *amplitude* as the experimental deformed shapes, which may be at a different *frequency* in places where the numerical and experimental backbones do not perfectly overlap. The points at which the deformed shapes are taken are marked with circles in Figs. 9(a), 10(a) and 11(b,d). The numerical deformed shape is then overlaid onto the experimental deformed shape tracked by the camera, as seen in Fig. 13 and Fig. 14.

The deformed shape is not traced for all three beams on all three modes. Recall from Section 5.1 that η does not have an influence on the nonlinear modes since it is very small for all three beams, and from [19] that α, which only affects the first nonlinear mode, does not change the nonlinear mode shape. For these reasons, it is sufficient to trace the nonlinear deformed shape for only one
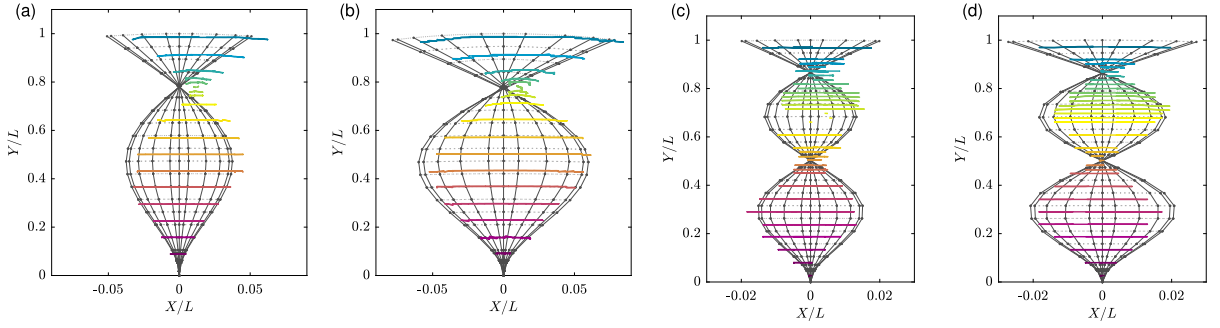
Fig. 14. Deformed shape of the second nonlinear mode of beam 3 for several base accelerations. (a): point A of Figs. 11(c); (b): point B. Notice that the scale is different in X and Y axes.
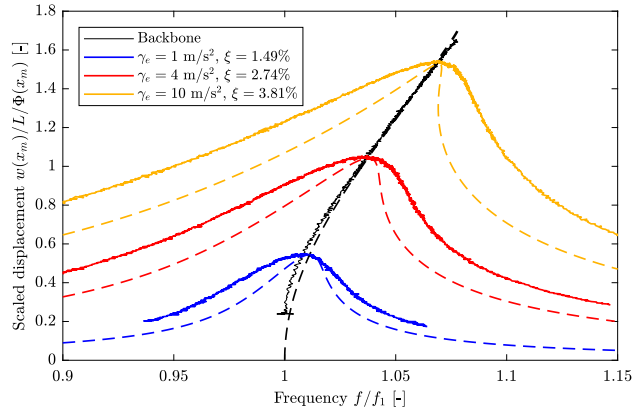

Fig. 15. Experimental frequency response and backbone curves of mode 1 of beam 1 (same as Fig. 9(a)) compared to the numerical model, shown in dashed line. The damping ratio ξ of the linear mass proportional damping model for the numerical computations of the forced frequency responses is different for each forcing, adjusted to have the same resonance point in theory and experiments.

beam on each nonlinear mode. Comparing these figures, globally there is very good agreement between the experimental and numerical deformed shapes. This is especially true on the first nonlinear mode in Fig. 13, where the experimental mode shape is nearly identical to the experimental one even at very large amplitudes. On the higher nonlinear modes 2 and 3, some points are not perfectly aligned in the mode shape, due to slightly curved equilibrium positions and to difficulties in the tracking software since the amplitudes are much smaller than on the first nonlinear mode. Overall, however, excellent agreement with the numerical mode shapes and an accurate representation of the known nonlinear mode shapes are found on all three nonlinear modes.

5.4. Damping estimation

In contrast to the two previous sections that were dedicated to conservative properties of the beams under study (backbone curves and nonlinear deformed shapes of CNMs), we now consider the dissipation of energy that occurs during the oscillations of the structure due to the effects of damping. Whereas inertia and elasticity are characterized by very accurate models, damping can be caused by a large variety of distinct phenomena (internal thermoelastic or viscoelastic dissipation [99], aeroelastic drag [4], anchor losses in M/NEMS [100], among others). They can be intrinsically nonlinear (such as the aeroelastic drag), but can also be associated with a linear stress/strain law manifesting nonlinear damping effects when mixed with geometrical nonlinearities (see Appendix A.2 or [60,87]). Such effects can also combine together, such that an accurate and predictive model is often out of reach. When the damping effect is linear, a modal viscous damping model is often sufficient and the associated damping factor (or quality factor) can be easily estimated experimentally using a half power bandwidth method or more advanced modal extraction parameter methods [101]. In the case of nonlinear damping effects, however, a general model does not exist; an experimental method is proposed here to estimate a damping law as a *by-product* of the phase resonance measurement of the conservative nonlinear mode.

As explained in Section 2, phase resonance allows for natural separation of the conservative and dissipative parts of the dynamics. Whereas the backbone curves and the nonlinear mode shapes investigated in Sections 5.2 and 5.3 are related to the conservative forces, the dissipative part is related to the damping forces, exactly balanced by the forcing under phase resonance conditions (see Eq. (12)). By consequence, plotting the forcing as a function of the amplitude of the motion can serve as a way of investigating the damping.
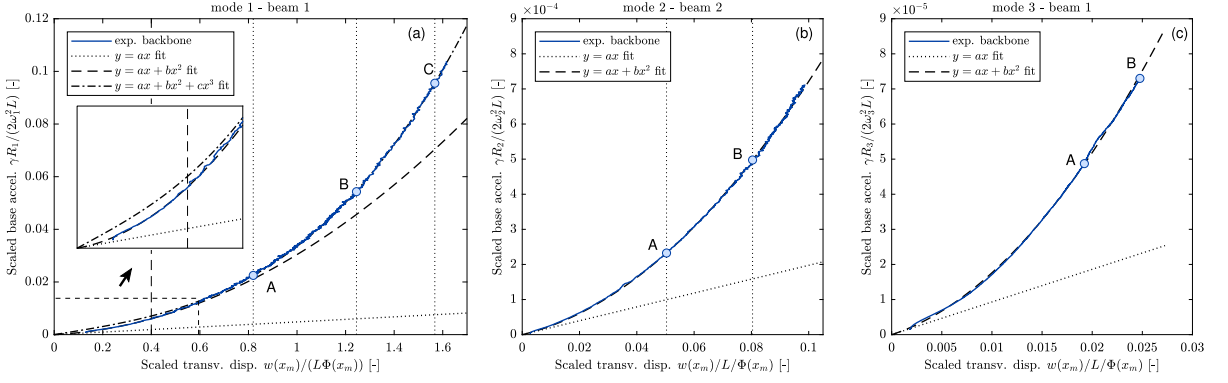
Fig. 16. Base acceleration as a function of the amplitude of beam 1 on the backbone curve and several polynomial fits. (a): mode 1 of Fig. 9(a); (b): mode 2 of Fig. 11(b); (c): mode 3 of Fig. 11(d). The vertical dashed black line in (a) shows the upper limit of the experiments of [4]. The letters A, B, C refer to the mode shapes of Fig. 13.
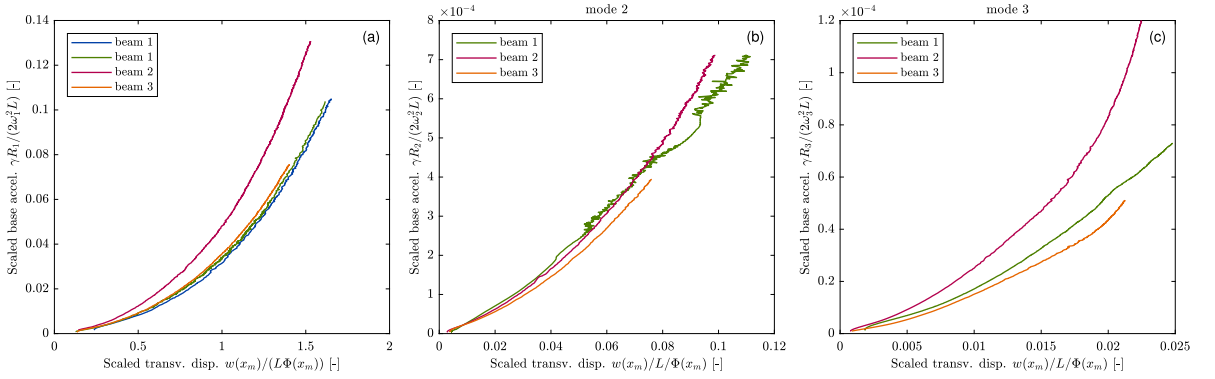

Fig. 17. Scaled base acceleration as a function of the scaled amplitude on the backbone curve compared for several beams and a given mode, from Figs. 9 and 11; (a): mode 1; (b): mode 2; (c): mode 3.

A first investigation into the nonlinear nature of the damping of the measured cantilevers is shown in Fig. 15. In it, the three experimental frequency responses of Fig. 9(a) are compared to three numerical computations using the method of [19], as described in Section 3.1. More precisely, Eq. (13) is solved in the frequency domain with a mass proportional *linear* damping model, namely $D = 2\omega_1 \xi M$ with ω_1 the first natural frequency and ξ the damping ratio. For each value of the base acceleration amplitude γ_e, the damping ratio is adjusted such that the experimental and numerical frequency response curves coincide at the resonance point. This method leads to three distinct values of ξ (see the legend of Fig. 15) and a significant discrepancy between the curves at any point away from the resonance. It is clear from Fig. 15 that this simple damping model is far from representing reality.

Nevertheless, the losses can be characterized as a function of the amplitude of the motion using the data associated with the phase resonance computation/measurement of the backbone curve of the CNM in the same way as in Section 3.3. This is investigated in Fig. 16 using the data of the phase resonance testing of beam 1 (Fig. 9(a) for mode 1, Fig. 11(a) for mode 2 and Fig. 11(d) for mode 3) by plotting the first harmonic of the scaled base acceleration as a function of the first harmonic of the scaled transverse displacement of the beam at x_m (refer to Section 4.4 for details about the scaling). The experimental curves, depicted in blue, indicate significant nonlinear behavior, which was previously discussed in Section 3.3. To characterize these nonlinearities, the experimental curves are fitted with three polynomial models, shown in black: linear (dotted curve), quadratic (dashed curve) and cubic (dash-dotted curve).

For mode 1 (Fig. 16(a)), the polynomial fits indicate that the linear model only explains the tangent to the curve at zero amplitude as the trend is immediately dominated by a strong quadratic effect. This trend was also observed in [4] using the same kind of cantilever beam experiments; in [4] the quadratic trend was explained as an aeroelastic drag effect due to the air-structure interaction during the motion. Then, at larger amplitude, for $w_m/(L\Phi(x_m)) > 0.5$, an additional cubic effect is observed, likely related to the geometrical nonlinearities that mix with other damping effects as discussed in Section 3.3. Note that this cubic damping response at large amplitude was not observed in [4] since the experiments were restricted to a moderate amplitude of vibration, shown in Fig. 16(a) with a vertical dashed black line at $w_m/(L\Phi(x_m)) \simeq 0.4$, which is below the onset of the cubic trend. This cubic trend is in accordance with past results of the literature [21,60,87–90]. However, the coexistence of both quadratic and cubic trends is, to our knowledge, an original observation.

On the higher nonlinear modes 2 and 3, the blue experimental curves follow the quadratic (dashed curve) trend, which agrees with the previous observations since the amplitude of the scaled transverse displacement on these modes remains below the limit of [4].

To conclude, the above investigations imply that the damping encountered in the experiments is likely dominated by a quadratic aeroelastic drag, observed on the three modes of beam 1. For extreme amplitudes of vibration, observed only on mode 1 where the amplitude is sufficiently large, a cubic effect is observed, likely explained as a combination of effects due to the geometrical nonlinearities and some damping effects. As a final insight, Fig. 17 collects the same plots obtained for the three beams of different geometries (see Table 1). While beam 2 manifests a larger quadratic damping than the other two beams, the discussion is postponed to future work since quadratic drag is related to complex fluid–structure phenomena extending beyond the scope of the present work.

6. Conclusion

In this work, the results of phase resonance testing of highly flexible cantilevers have been presented and discussed at length. The results are separated into two distinct categories: conservative and dissipative effects. In the former, the idea of phase resonance has been used by way of a Phase-Locked Loop controller for the experimental measurement of conservative nonlinear modes. In particular, we are interested in measuring the experimental CNMs of highly flexible structures at very large amplitudes of vibration. To this end, the first three CNMs of slender cantilever rulers excited via base acceleration are measured and used to validate the numerical model of previous work (in particular [19]). Globally, good agreement is found between the experimental and numerical CNMs, such that the numerical model is validated when some important considerations, such as the effect of gravity and potential ribbon effects, are also taken into account. Then, the phase resonance testing of the cantilever beams is used to estimate the nonlinear damping at very large amplitudes. It is shown numerically in Section 3.3 and experimentally in Section 5.4 that the damping (in open air experiments) is nonlinear, in agreement with previous work [4,21]. Moreover, it is shown that the damping transitions from being linear at very small amplitudes to quadratic at moderate amplitudes, cubic at large amplitudes and even higher order at extreme amplitudes of motion.

The PLL technique, though applied here to a highly flexible beam, may be applied with no restriction to measure the CNMs and the damping law of any linear and nonlinear system, whether it is a more standard engineering structure with small deformations like an airplane [72] or a multibody system such as nonlinear isolators [102]

In future work, we aim to continue the experiments in order to further the damping investigation; one potential option in this regard is to redo similar experiments within a vacuum as done in [21] in order to minimize the air drag of open air experiments. In addition, more work is needed in order to fully characterize the behavior of the CNMs on the second and third nonlinear modes. In particular, we seek to explain the discrepancy between the backbones of beam 1 on these modes (either through an improved understanding of the ribbon effects or by other means). Finally, the topics and experiments of this chapter can be extended to other flexible systems in future work, such as experiments involving the flexible ring of [18] or investigating the parametric behavior of flexible cantilevers [26,103].

CRediT authorship contribution statement

Marielle Debeurre: Writing – review & editing, Writing – original draft, Validation, Software. **Simon Benacchio:** Validation, Investigation, Data curation. **Aurélien Grolet:** Supervision. **Clément Grenat:** Formal analysis. **Christophe Giraud-Audine:** Software, Investigation, Conceptualization. **Olivier Thomas:** Writing – review & editing, Supervision, Methodology, Funding acquisition, Data curation, Conceptualization.

Declaration of competing interest

The authors declare that they have no known competing financial interests or personal relationships that could have appeared to influence the work reported in this paper.

Data availability

Data will be made available on request.

Acknowledgments

Appendix A. Some models with nonlinear damping and inertia

In this appendix, several models of the literature are recalled in order to show various forms of nonlinearities, both conservative and dissipative. In all cases, the model falls into the form of Eq. (1), with the conservative and dissipative vectors, respectively, odd and even functions of $\dot{x}$, as described in Section 2.4.

A.1. An elastic pendulum

Consider first the free oscillations of an elastic pendulum, composed of a mass m linked to a Galilean frame by a linear spring of stiffness k and unstretched length l_0, subjected to a plane motion in a vertical gravity field of acceleration g. Its two generalized coordinates are chosen as the angle $\theta(t)$ of the spring with the vertical and the length $\lambda(t)$ of the spring. The kinetic and potential energies are written as:

$$\mathcal{T} = \frac{1}{2}m\left(\dot{\lambda}^2 + \lambda^2\dot{\theta}^2\right), \quad \mathcal{V} = \frac{1}{2}k\left(\lambda - l_0\right)^2 - m\lambda g \cos\theta, \tag{A.1}$$

The equations of motion, obtained for instance with Lagrange equations, are in the form of Eq. (1) with:

$$x(t) = \begin{bmatrix} \theta(t) \\ \lambda(t) \end{bmatrix}, \quad M = \begin{bmatrix} m\lambda^2 & 0 \\ 0 & m \end{bmatrix}, \quad f_c = \begin{bmatrix} 2m\dot{\theta}\dot{\lambda}\lambda + m\lambda g \sin\theta \\ -m\dot{\theta}^2\lambda + k(\lambda - l_0) - mg\cos\theta \end{bmatrix}, \quad f_d = f_e = 0. \tag{A.2}$$

Notice the dependence of the inertia matrix on $\lambda(t)$ and the nonlinear quadratic (even) dependence of the conservative force vector f_c on $(\dot{\theta}, \dot{\lambda})$.

A.2. An inextensible beam model with viscous and Kelvin–Voigt damping

This section considers the addition of two well-known simple linear damping laws in the model for vibrations of a slender cantilever beam, mostly to observe how their interaction with the geometrical nonlinearities creates nonlinear damping terms. As initially introduced in [56] and with the same notations as in [7,19], we consider the vibrations of a slender cantilever beam of length L whose deformation is defined by the axial displacement field $u(x,t)$, the transverse displacement field $w(x,t)$ and rotation field $\theta(x,t)$ of the cross section at abscissa x and time t. The purpose of this section is to analyze the effect of damping in the equations.

With an inextensibility constraint $((1 + u')^2 + w'^2 = 1$, with $\circ' = \partial\circ/\partial x$), Euler–Bernoulli kinematics and neglected rotational inertia, the equations of motion can be written:

$$\rho A(\ddot{u} + \mu\dot{u}) = (N\cos\theta - T\sin\theta)', \quad \rho A(\ddot{w} + \mu\dot{w}) = (N\sin\theta + T\cos\theta)' + p, \quad T = -M', \tag{A.3}$$

where ρ is the density of the material, A the area of the cross section and (N, T, M) the generalized forces (axial force, transverse force, bending moment) and $p(x,t)$ is an external transverse force per unit length. Notice the *viscous damping term* introduced in both axial and transverse motion, of coefficient μ [s^{-1}].

As in [21,26], a *Kelvin–Voigt (KV) damping model* is added in the form $\sigma = E(\varepsilon + \tau\dot{\varepsilon})$, with σ the axial stress, ε the axial strain, E the Young's modulus of the material and τ a damping time constant. Considering the geometrically exact model with an inextensible centerline, $\varepsilon = -z\theta'$ with z the transverse coordinate of any point in the cross section. Then, considering the definitions of M as an integral of stress in the cross section, the following relation is obtained:

$$M = \int_A z\sigma \, dA = EI(\theta' + \tau\dot{\theta}'), \tag{A.4}$$

with I the second moment of area of the cross section. Then, as explained in [7,19], the above expression is introduced into the equations of motion (A.3), in which N is eliminated, to obtain only one equation for the bending motion of the beam:

$$\rho A(\ddot{w} + \mu\dot{w}) + EI\left(\frac{\theta''}{\cos\theta}\right)' + \tau EI\left(\frac{\dot{\theta}''}{\cos\theta}\right)' - \rho A\left(\tan\theta\int_L^X (\ddot{u} + \mu\dot{u}) \, dX\right)' = p. \tag{A.5}$$

The inextensibility condition leads to $\sin\theta = w'$, $\cos\theta = 1 + u'$, $u' = \sqrt{1 - w'^2} - 1$. Finally, eliminating u and θ as functions of w and performing Taylor expansions in w up to order three, it is possible to obtain a model cubic in $w(x,t)$:

$$\rho A(\ddot{w} + \mu\dot{w}) + EI\left[w'''' + (w'w''^2 + w'''w'^2)'\right] + \tag{A.6}$$

$$\tau EI\left[\dot{w}'''' + \dot{w}'(w'w''' + w''^2) + 2\dot{w}''w'w'' + \dot{w}'''w'^2\right]' + \frac{\rho A}{2}\left[w'\int_L^x\left(\frac{\partial^2}{\partial t^2} + \mu\frac{\partial}{\partial t}\right)\int_0^x w'^2 \, dx \, dx\right] = p.$$

To analyze the effect of the damping, it is convenient to expand this partial differential equation on a given vibration mode: $w(x,t) = \Phi(x)q(t)$. Using the orthogonality of Φ, one obtains:

$$\ddot{q} + 2(\mu + \tau\omega_0^2)\dot{q} + (\mu\Lambda + \tau\Delta)q^2\dot{q} + \omega_0^2 q + \Gamma q^3 + \Pi(\dot{q}^2 + q\ddot{q})q = Q, \tag{A.7}$$

where ω_0 is the natural frequency of the considered mode and (Γ, Π) are the classical nonlinear coefficients (see *e.g.* [7,19]). This equation is in the form of Eq. (1) with $x = [q]$. The viscous damping (proportional to μ) adds a linear term, but also a nonlinear

term proportional to the coefficient Λ because of the axial motion condensation. The KV damping (proportional to τ) further adds a linear term and also a nonlinear term proportional to coefficient Δ. These two nonlinear damping contributions are both cubic (of the form $q^2\dot{q}$) and stem from the joint contribution of the damping models, both linear, with the geometrical nonlinearities. This result has been identified and analyzed in [60] and is illustrated in Fig. 2. As shown in Section 2.4, it is observed that the conservative terms have an *even* dependence in $\dot{q}$ through the term $\Pi\dot{q}^2q$, whereas the dissipative terms are *odd* in $\dot{q}$ (they are all proportional to $\dot{q}$).

A.3. A cantilever beam with quadratic aeroelastic drag

It is possible to include in the model of a vibrating structure the damping effect of an aeroelastic drag, proportional to the square of the velocity as shown in [4]. In [4], a term of the form $f_{ae} = v\dot{q}|\dot{q}|$ is added *a posteriori* in Eq. (A.7). As described in Section 2.4, this term is an odd function of $\dot{q}$ since $f_{ae}(-\dot{q}) = -f_{ae}(\dot{q})$ (due to the absolute value).

A.4. An energy harvester with material piezoelectric nonlinearities

When a mechanical structure includes a piezoelectric material, particular nonlinearities (both conservative and dissipative) due to ferroelastic hysteresis behavior have to be taken into account. A model for such a structure, restricted to one of its vibration modes and coupled to an electric resistor R for energy harvesting applications, is considered in [61]. It can be written in the form of Eq. (1) with:

$$x(t) = \begin{bmatrix} u(t) \\ Q(t) \end{bmatrix}, \quad M = \begin{bmatrix} m & 0 \\ 0 & 0 \end{bmatrix}, \quad f_c = \begin{bmatrix} k_1 u + k_2 u^2 \mathrm{sgn}(u) - [\theta_1 + \theta_2 u \mathrm{sgn}(u)] Q/C \\ Q - [\theta_1 + \theta_2 u \mathrm{sgn}(u)/2] u \end{bmatrix}, \tag{A.8}$$

$$f_d = \begin{bmatrix} [c_1 u \mathrm{sgn}(u) + c_2 u^2] \mathrm{sgn}(\dot{u}) \\ RC\dot{Q} \end{bmatrix}, \quad f_e = \begin{bmatrix} F(t) \\ 0 \end{bmatrix}, \tag{A.9}$$

where $\mathrm{sgn}(\circ)$ is the sign of function $\circ(t)$. The unknowns are the mechanical modal coordinate $u(t)$ and the electric charge $Q(t)$. C is the electric capacitance of the piezoelectric elements, m the modal mass, (c_1, c_2) damping coefficients, (k_1, k_2) stiffness coefficients, (θ_1, θ_2) piezoelectric coupling coefficients and $F(t)$ the external mechanical force. Here, the dissipative factor f_d is an odd function of $\dot{x} = [\dot{u}\ Q]^T$.

Appendix B. A cantilever beam into base acceleration

We consider the geometrically exact equations of motion of a cantilever beam (A.3) and we separate the absolute transverse displacement field $w(x,t)$ into the prescribed base displacement $w_b(t)$ and the relative displacement field $w_r(x,t)$, such that $w(x,t) = w_b(t) + w_r(x,t)$. The two other fields $u(x,t)$ and $\theta(x,t)$ remain unchanged. Then, the second equation becomes:

$$\rho A(\ddot{w}_r + \mu\dot{w}_r) = (N\sin\theta + T\cos\theta)' + p - \rho A\ddot{w}_b, \tag{B.1}$$

Then, one easily observes that $w_r(x,t)$ exactly replaces $w(x,t)$ in the equations of motions, and that the external forcing can be identified as $p(x,t) = -\rho A\gamma(t)$: a uniformly distributed force proportional to the base acceleration $\gamma(t) = \ddot{w}_b(t)$.

To analyze quantitatively the motion of the beam, it is convenient to have an idea of its motion in the simple case of (small amplitude) linear vibrations, with a simple viscous modal damping model. Under this assumption, the transverse relative displacement, reduced to a single mode motion, can be written:

$$w_r(x,t) = \Phi_k(x)q(t), \quad \ddot{q} + 2\xi_k\omega_k\dot{q} + \omega_k^2 q = Q(t), \quad Q(t) = \frac{\int_0^L \Phi_k(x)p(x,t)\,\mathrm{d}x}{\int_0^L \rho A\Phi_k^2(x)\,\mathrm{d}x}. \tag{B.2}$$

Under base harmonic acceleration $\gamma(t) = \gamma_e\cos\omega t$, at the phase resonance ($\omega = \omega_k$),

$$w_r(x,t) = w_1(x)\cos(\omega t - \pi/2), \quad w_1(x) = \frac{R_k\Phi_k(x)\gamma_e}{2\xi_k\omega_k^2}, \quad R_k = \frac{\int_0^L \Phi_k(x)\,\mathrm{d}x}{\int_0^L \Phi_k^2(x)\,\mathrm{d}x}, \tag{B.3}$$

where R_k depends on the mode shape $\Phi_k(x)$ of the cantilever beam. With the following normalization $\int_0^L \Phi_k^2(x)\,\mathrm{d}x = 1$, $R_1 = 1.566$, $R_2 = 0.8678$ and $R_3 = 0.5088$. Then, the scaled displacement at any point of the beam writes:

$$\frac{w_1(x)}{L\Phi_k(x)} = \frac{w_1(x_m)}{L\Phi_k(x_m)} = \frac{w_1(L)}{L} = \frac{R_k\gamma_e}{2L\xi_k\omega_k^2}. \tag{B.4}$$

Appendix C. Justification of a monophase CNM motion

We assume that the conservative force vector $\boldsymbol{f}_{\mathrm{c}}(\boldsymbol{x}, \dot{\boldsymbol{x}})$ and the mass matrix $\boldsymbol{M}(\boldsymbol{x})$ are smooth around the equilibrium point $(\boldsymbol{x}, \dot{\boldsymbol{x}}) = (\boldsymbol{0}, \boldsymbol{0})$ and that the $\dot{\boldsymbol{x}}$ dependence is even, such that their Taylor expansions can be written, in index notation:

$$M_{ij}(\boldsymbol{x}) = M_{ij}^{(0)} + M_{ijk}^{(1)} x_k + M_{ijkl}^{(2)} x_k x_l + M_{ijklm}^{(3)} x_k x_l x_m + \cdots \tag{C.1}$$

$$[\boldsymbol{f}_{\mathrm{c}}(\boldsymbol{x}, \dot{\boldsymbol{x}})]_i = K_{ij}^{(1)}(\dot{\boldsymbol{x}}) x_j + K_{ijk}^{(2)}(\dot{\boldsymbol{x}}) x_j x_k + \cdots, \tag{C.2}$$

$$K_{ij}^{(1)}(\dot{\boldsymbol{x}}) = K_{ij}^{(1,0)} + K_{ijkl}^{(1,2)} \dot{x}_k \dot{x}_l + \cdots \tag{C.3}$$

$$K_{ijk}^{(2)}(\dot{\boldsymbol{x}}) = K_{ijk}^{(2,0)} + K_{ijklm}^{(2,2)} \dot{x}_l \dot{x}_m + \cdots, \tag{C.4}$$

where the index i, j, k, l, m are integers, $f_i = [\boldsymbol{f}]_i$ is the ith component of vector $\boldsymbol{f}$ and $M_{\bullet}^{(\bullet)}$, $K_{\bullet}^{(\bullet)}$ are the components of high order matrices corresponding to the coefficients of the Taylor expansions. Analyzing these expressions, it can be concluded that their time dependencies appear through products of the components of $\boldsymbol{x}(t)$ of arbitrary order and components of $\dot{\boldsymbol{x}}(t)$ of even order only. For the particular case of the motion onto the ith "linear" mode defined by Eq. (5) (we omit here the i and "lm" indices in what follows in order to simplify the writing), the following relations are found:

$$\boldsymbol{x}(t) = \boldsymbol{\Phi} \cos \omega t \quad \Rightarrow \quad \left\{ \begin{array}{l} x_k(t) = \Phi_k \cos \omega t \\ \dot{x}_k(t) = -\omega \Phi_k \sin \omega t \end{array} \right. \quad \forall k = 1 \ldots N. \tag{C.5}$$

Then, considering the trigonometric relations:

$$\sin^2 \theta = (1 - \cos 2\theta)/2, \quad \sin^4 \theta = (3 - 4 \cos 2\theta + \cos 4\theta)/8, \tag{C.6}$$

$$\cos^2 \theta = (1 + \cos 2\theta)/2, \quad \cos^3 \theta = (3 \cos \theta + \cos 3\theta)/4, \tag{C.7}$$

that contain only $\cos h\theta$ ($h \in \mathbb{N}^*$), the product of $\cos(\omega t)$, to any power, with $\sin(\omega t)$, to any even power, is found to produce only $\cos(h\omega t)$ terms in its Fourier expansion. Consequently, the conservative forces in Eq. (1) $\boldsymbol{M}(\boldsymbol{x})\ddot{\boldsymbol{x}}$ and $\boldsymbol{f}_{\mathrm{c}}(\boldsymbol{x}, \dot{\boldsymbol{x}})$ produce only $\cos(h\omega t)$ and thus only in-phase harmonics, in the case of a given "linear" mode motion as written in Eq. (6).

Appendix D. Monophase motion and internal resonance

The monophase property of a given CNM clearly holds in the main parts of a given backbone curve, but it is worth investigating if this property is maintained in the presence of internal resonances. We first consider internal resonances which are observed far from the equilibrium point, if commensurable relationships appear between the nonlinear modal frequencies of several modes. These internal resonance often appear as "tongues" or branches that emanate from the backbone branch [27].

As an example, consider the two degree-of-freedom system considered in [27]:

$$\ddot{x}_1 + (2x_1 - x_2) + 0.5x_1^3 = 0, \quad \ddot{x}_2 + (2x_2 - x_1) = 0. \tag{D.1}$$

The first CNM of Eq. (D.1), of natural frequency $\omega_1 = 1$, is computed by numerical continuation of periodic solutions using the MANLAB software as explained in [104]. It allows for computation of the sine and cosine components of the variables, such as:

$$x(t) = \hat{x}_0 + \sum_{h=1}^{H} \left(\hat{x}_h^{\mathrm{c}} \cos \omega t + \hat{x}_h^{\mathrm{s}} \sin \omega t \right), \tag{D.2}$$

for a variable $x(t)$. In our simulations, the phase condition is prescribed as $\hat{x}_1^{\mathrm{s}} = 0$ (the sine component of the first harmonic of $x_1(t)$ is enforced to be zero). Fig. D.18(a) shows the backbone curve of the first CNM in a frequency energy plot in the vicinity of the 1:2 and 1:3 internal resonances. Figs. D.18(b),(c) and (d) depict the sine and cosine of the first three harmonics of $x_1(t)$.

In Figs. D.18(b)–(d), it is first noted that the main backbone branch (called branch 1) is perfectly monophase since all sine components are zero on this branch. Analogous figures, not reported here for the sake of brevity, are obtained for $x_2(t)$. The periodic solution in branch 1 thus naturally verifies Eq. (4). Remarkably, this property still holds in the 1:3 internal resonance branches, which are also monophase.

The case of the 1:2 internal resonance tongue is slightly different. The corresponding branches are obtained after symmetry breaking (pitchfork) bifurcations of branch 1 (points A and B), leading to two bifurcated branches (branches 2 and 3) with additional even harmonics with respect to branch 1 (all even harmonics in branch 1 are zero since the nonlinearities in Eq. (D.1) are cubic only). In this case, the motion is monophase (it verifies Eq. (4)) only in the right part of the branches, between points B and C. In the other part (between points A and C), the harmonic 2 sine component is nonzero with a zero cosine component, leading to a motion of the form:

$$\boldsymbol{x}_{1:2}(t) = \hat{\boldsymbol{x}}_0 + \hat{\boldsymbol{x}}_1 \cos \omega t + \hat{\boldsymbol{x}}_2 \sin 2\omega t + \hat{\boldsymbol{x}}_3 \cos 3\omega t + \hat{\boldsymbol{x}}_4 \sin 4\omega t + \cdots, \tag{D.3}$$

which *is not* a monophase CNM since the even harmonics are in quadrature with respect to the odd ones.

Monophase and non-monophase CNMs with components in quadrature are also classical in the case of internal resonances that appear at low amplitude, if the commensurable relations are verified between the natural frequencies of the system. In the case of a 1:1 internal resonance between two modes of a system with cubic nonlinearities (their natural frequencies being written
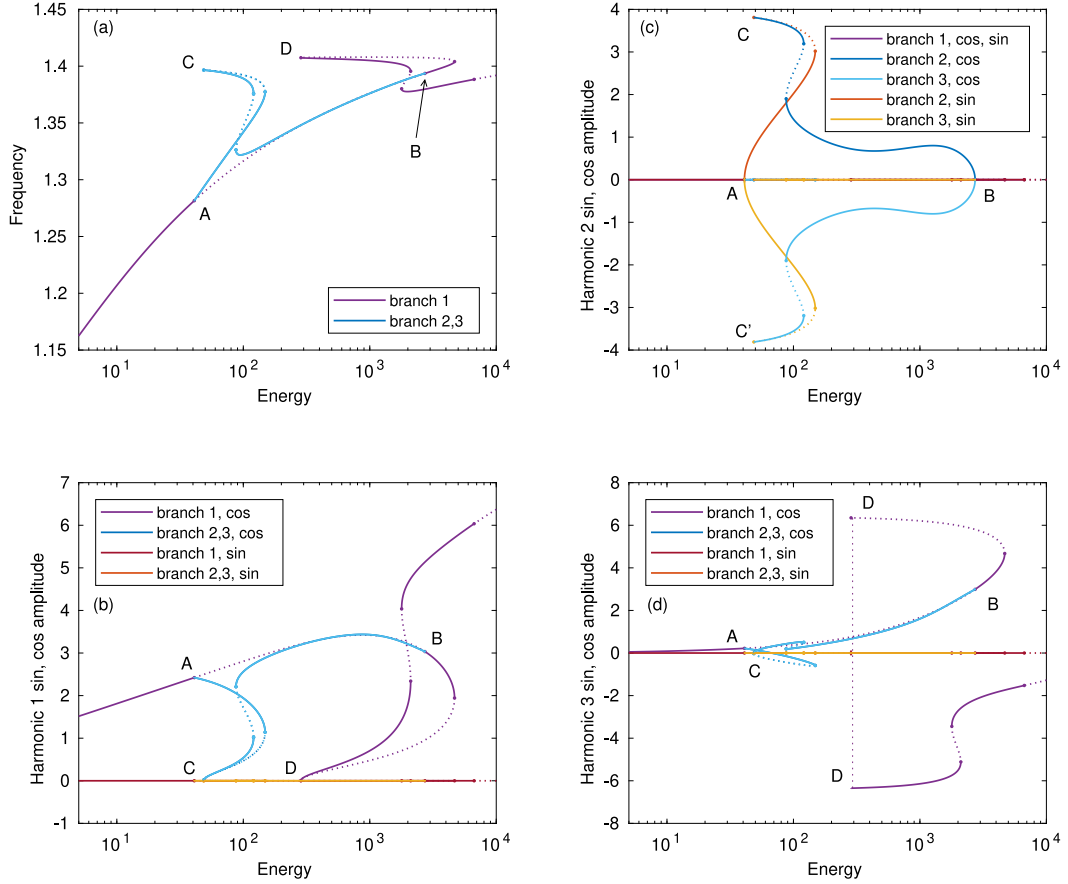
Fig. D.18. Backbone curve of mode 1 of the two degrees-of-freedom system of Eq. (D.1). (a) Frequency-energy plot; (b,c,d) cosine and sine components of harmonic 1, 2, 3 of $x_1(t)$ as a function of the energy. A and B are two symmetry breaking pitchfork bifurcations, between the main branch with odd only harmonics (branch 1) and the two bifurcated branches of the 1:2 internal resonance (branch 2, 3) with even harmonics in addition. C and D are the connections between CNM 1 and CNM 2 (see [13]).

$\omega_1 \simeq \omega_2$), there are two possible coupled modes [41]. The former, called a "normal mode," is characterized by the two modal coordinates oscillating in phase or out of phase (see Eq. (16) of [41]); it is therefore a monophase CNM. In the latter, called an "elliptic mode," the two modal coordinates are in phase quadrature; it is therefore not a monophase CNM. Another example is found for the case of a system with quadratic nonlinearities and two modes in 1:2 internal resonance (their natural frequencies being written $\omega_2 \simeq 2\omega_1$) [70]. In this case, the coupled CNM, called "parabolic modes," are characterized by a phase quadrature, similar to Eq. (D.3) (see Eq. (21) of [70]).

Appendix E. Odd and even parts of the forces vectors with a monophase motion

Due to the parity of $f_c(\boldsymbol{x}, \dot{\boldsymbol{x}})$ and $f_d(\boldsymbol{x}, \dot{\boldsymbol{x}})$ as in Appendix C, their Taylor expansions are of the form:

$$[\boldsymbol{f}_c(\boldsymbol{x}, \dot{\boldsymbol{x}})]_i = \tilde{f}_i^{(0)}(\boldsymbol{x}) + \tilde{K}_{ijk}^{(2)}(\boldsymbol{x})\dot{x}_j \dot{x}_k + \cdots, \tag{E.1}$$

$$[\boldsymbol{f}_d(\boldsymbol{x}, \dot{\boldsymbol{x}})]_i = D_{ij}^{(1)}(\boldsymbol{x})\dot{x}_j + D_{ijkl}^{(3)}(\boldsymbol{x})\dot{x}_j \dot{x}_k \dot{x}_l + \cdots, \tag{E.2}$$

where $\tilde{f}_i^{(0)}(\boldsymbol{x})$, $\tilde{K}_\bullet^{(\bullet)}(\boldsymbol{x})$, $D_\bullet^{(\bullet)}(\boldsymbol{x})$ are the components of high order matrices corresponding to the coefficients of the Taylor expansions in $\dot{\boldsymbol{x}}$, all arbitrary smooth functions of $\boldsymbol{x}$. The tilde notation is used to distinguish the coefficients from those of Eq. (C.2).

We consider the particular monophase motion Eq. (4) of a CNM. As it contains only $\cos(h\omega t)$ components and because of the following trigonometric identity:

$$\cos(n\theta)\cos(m\theta) = (\cos[(m+n)\theta] + \cos[(m-n)\theta])/2, \quad \forall n, m \in \mathbb{N}, \tag{E.3}$$

the Fourier expansion of any product of any order $[\boldsymbol{x}_{cnm}]_i[\boldsymbol{x}_{cnm}]_j$, $[\boldsymbol{x}_{cnm}]_i[\boldsymbol{x}_{cnm}]_j[\boldsymbol{x}_{cnm}]_k, \ldots$ of the components of $\boldsymbol{x}_{cnm}$ is monophase and contains only $\cos(h\omega t)$ components. This is also the case for the Fourier expansions of $\tilde{f}_i^{(0)}(\boldsymbol{x})$, $\tilde{K}_\bullet^{(\bullet)}(\boldsymbol{x})$, $D_\bullet^{(\bullet)}(\boldsymbol{x})$ since their Taylor expansions in $\boldsymbol{x}$ are of the form of Eq. (C.1).

In addition, $\dot{x}_{\text{cnm}}$ is monophase with only $(\sin h\omega t)$ components:

$$\dot{x}_{\text{cnm}}(t) = -\sum_{h=1}^{H} h\omega \hat{x}_h \sin(h\omega t). \tag{E.4}$$

The Fourier expansion of *even order products* of the components of $\dot{x}_{\text{cnm}}$ contain only $\cos(h\omega t)$ components, whereas *odd order products* of the components of $\dot{x}_{\text{cnm}}$ contain only $\sin(h\omega t)$ components, due the following trigonometric identity, $\forall n, m \in \mathbb{N}$:

$$\sin(n\theta)\sin(m\theta) = (\cos[(m-n)\theta] - \cos[(m+n)\theta])/2, \tag{E.5}$$

$$\sin(n\theta)\cos(m\theta) = (\sin[(m+n)\theta] - \sin[(m-n)\theta])/2. \tag{E.6}$$

As a consequence, the Fourier expansion of the *conservative* force vector is monophase and contains only $\cos(h\omega t)$ components, while the Fourier expansion of the *dissipative* force vector (also monophase) contains only $\sin h\omega t$ components:

$$f_{\text{c}}(x, \dot{x}) = \hat{f}_{\text{c}0} + \sum_{h=1}^{H} \hat{f}_{\text{c}h} \cos(h\omega t), \quad f_{\text{d}}(x, \dot{x}) = \sum_{h=1}^{H} -\hat{f}_{\text{d}h} \sin(h\omega t). \tag{E.7}$$

Notice the - sign in the f_{d} components, to be coherent with Eq. (E.4). In particular, in the case of a linear damping, the dissipative force vector onto a CNM motion reads:

$$f_{\text{d}} = D\dot{x}_{\text{cnm}} = -\sum_{h=1}^{H} h\omega D\hat{x}_h \sin(h\omega t). \tag{E.8}$$

Appendix F. Odd and even parts of the motion for a geometrically nonlinear straight beam

As in Appendix A.2, we consider the free conservative vibration of a straight beam based on a geometrically exact model with Euler–Bernoulli kinematics (Timoshenko kinematics, not investigated here for the sake of brevity, would lead to exactly the same results with the same reasoning). The equations of motion are (A.3), with $\mu = 0$ to cancel the damping and, from [7]:

$$N = EA\left[(1 + u')\cos\theta + w'\sin\theta - 1\right], \quad M = EI\theta'. \tag{F.1}$$

The equations of motion can be rewritten as $\ddot{u} = f_u(u, w, \theta)$ and $\ddot{w} = f_w(u, w, \theta)$, with $\sin\theta = w'$ and $\cos\theta = 1 + u'$ because of the Euler–Bernoulli kinematics. Observing the definition of f_u and f_w with Eqs. (A.3) and (F.1), it is clear that $f_u(u, -w, -\theta) = f_u(u, w, \theta)$ is even in (w, θ) and $f_w(u, -w, -\theta) = -f_u(u, w, \theta)$ is odd in (w, θ). With the reasoning of Appendix C, these parity properties lead to the following Taylor expansions:

$$f_u(u, w, \theta) = f_u^{(0)}(u) + k_{uww}^{(2)}(u)w^2 + k_{uw\theta}^{(2)}(u)w\theta + k_{u\theta\theta}^{(2)}(u)\theta^2 + k_{uw\theta}^{(2)}(u)w\theta + k_{uwwww}^{(4)}(u)w^4 + \cdots, \tag{F.2}$$

$$f_w(u, w, \theta) = k_{ww}^{(1)}(u)w + k_{w\theta}^{(1)}(u)\theta + k_{wwww}^{(3)}(u)w^3 + k_{www\theta}^{(3)}(u)w^2\theta + \cdots, \tag{F.3}$$

where $f_u^{(0)}(u)$, $k_{u\bullet}^{(\bullet)}$, $k_{w\bullet}^{(\bullet)}$ are the coefficients of the Taylor expansions. Consequently, $f_u(u, w, \theta)$ is quadratic in (w, θ) whereas $f_w(u, w, \theta)$ is cubic in (w, θ) (see Fig. F.19).

Finally, we consider the case of the motion onto a particular bending mode of the beam:

$$\begin{bmatrix} u(x, t) \\ w(x, t) \\ \theta(x, t) \end{bmatrix} = \begin{bmatrix} 0 \\ \Phi_w(x) \\ \Phi_\theta(x) \end{bmatrix} \cos(\omega t), \tag{F.4}$$

in which there is no axial motion because the beam is straight. Introducing these equations into the Taylor expansions Eqs. (F.2) and (F.3)), it is shown using Eq. (C.7) that f_u is monophase (in the form of Eq. (4)) with even harmonics only, whereas f_u (also monophase) has only odd harmonics. By consequence, an acceptable form for the axial, transverse and rotation fields of the CNM of a straight beam are:

$$u(x, t) = \hat{u}_0(x) + \hat{u}_2(x)\cos 2\omega t + \hat{u}_4(x)\cos 4\omega t + \cdots, \tag{F.5}$$

$$w(x, t) = \hat{w}_1(x)\cos\omega t + \hat{w}_3(x)\cos 3\omega t + \cdots, \qquad \theta(x, t) = \hat{\theta}_1(x)\cos\omega t + \hat{\theta}_3(x)\cos 3\omega t + \cdots.$$

This property is a direct consequence of the straight geometry of the beam and would be violated with a non-zero curvature.

Appendix G. Material parameters estimation

To estimate the value of the material parameters (Young's modulus E and density ρ), tensile tests were performed on two 300×13 rulers: one from the VMADE brand (the material of beam 1) and one from the FACOM brand (the material of beams 2 and 3). The traction machine enables measurement of different values of the traction force F and the resulting strain ε. With a linear fit, the value of the slope coefficient $\gamma_{F\varepsilon} = F/\varepsilon$ is estimated. The mass m of each ruler is measured with a precision scale along with the area A_{top} of its top surface and its width b. Then, the ratio E/ρ, which notably does not depend on the thickness h of the rulers (itself a source of uncertainty), is estimated as:

$$E = \frac{\gamma_{F\varepsilon}}{bh}, \quad \rho = \frac{m}{hA_{\text{top}}} \quad \Rightarrow \quad \frac{E}{\rho} = \frac{\gamma_{F\varepsilon}A_{\text{top}}}{bm}. \tag{G.1}$$
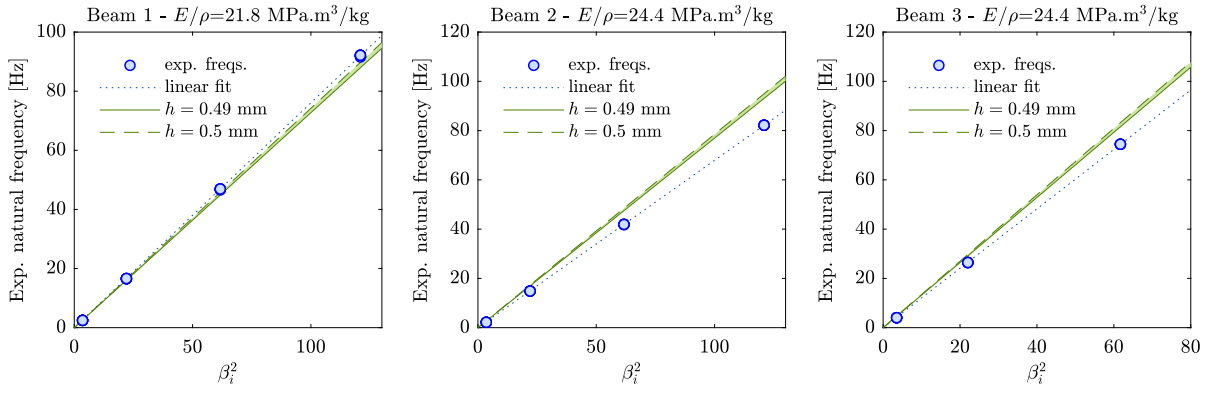
Fig. F.19. Experimental natural frequencies of the three beams as a function of the theoretical frequency parameters β_i^2 of a cantilever beam. Comparisons with theoretical values with E/ρ of Table 1 and $h \in \{0.49\ 0.5\}$ mm.

Table H.3
Maximum values of the curvature κ and the dimensionless ribbon parameter $\bar{\kappa} \simeq \frac{\kappa b^2}{h}$ for each beam $1-3$ on nonlinear modes $1-3$.

	Beam 1	Beam 2	Beam 3
Mode 1	$\kappa L = 5$ $\kappa = 13.2\ \text{m}^{-1}$ $\bar{\kappa} = 8.71$	$\kappa L = 5$ $\kappa = 13.2\ \text{m}^{-1}$ $\bar{\kappa} = 1.22$	$\kappa L = 5$ $\kappa = 17.2\ \text{m}^{-1}$ $\bar{\kappa} = 0.68$
Mode 2	$\kappa L = 1.5$ $\kappa = 3.95\ \text{m}^{-1}$ $\bar{\kappa} = 2.61$	$\kappa L = 1.5$ $\kappa = 3.95\ \text{m}^{-1}$ $\bar{\kappa} = 0.37$	$\kappa L = 1.5$ $\kappa = 5.17\ \text{m}^{-1}$ $\bar{\kappa} = 0.21$
Mode 3	$\kappa L = 1$ $\kappa = 2.63\ \text{m}^{-1}$ $\bar{\kappa} = 1.74$	$\kappa L = 1$ $\kappa = 2.63\ \text{m}^{-1}$ $\bar{\kappa} = 0.25$	$\kappa L = 1$ $\kappa = 3.45\ \text{m}^{-1}$ $\bar{\kappa} = 0.14$

The corresponding values of E/ρ are indicated in Table 1.

Then, the experimental natural frequencies of the three beams are compared to their theoretical value $\omega_i = \beta_i^2 h/L^2 \sqrt{E/(12\rho)}$, with $\beta_1 = 1.875$, $\beta_2 = 4.694$, $\beta_3 = 7.855$, $\beta_4 = 10.996$ [94] in Fig. F.19, showing a correct agreement.

Appendix H. Some details on ribbon effect

To further discuss the ribbon effect addressed in Section 5.2, the dimensionless parameter $\bar{\kappa}$ was estimated. Since it depends on κ, the effect should increase with the amplitude of the motion. To estimated the order of magnitude of $\bar{\kappa}$, we estimated the curvature κ at the clamp of the cantilever (it is its maximum value along the beam for all deformed shapes) at the top part of the experimental backbones curves of Figs. 9 and 11. It was easy since κ is one of the auxiliary unknown of the finite-element model [18]. The corresponding values of κ and $\bar{\kappa}$ are gathered in Table H.3. Since the backbone curves of all three beams reach approximately the same scaled amplitude, the scaled curvature κL is the same across all three beams, as shown in Table H.3. Then, because of the dependence of $\bar{\kappa}$ on L and b^2/h, different values of $\bar{\kappa}$ are obtained for each case. It is observed that $\bar{\kappa}$ is reduced for beam 2 and 3, indicating that the strongest ribbon effect, if any, should occur on beam 1, even if for the first mode, no discrepancy between experiments and theory is noticed.

References

[1] J.P. Cusumano, F.C. Moon, Chaotic non-planar vibrations of the thin elastica, part I: Experimental observation of planar instability, J. Sound Vib. 179 (2) (1995) 185–208.

[2] T.J. Anderson, A.H. Nayfeh, B. Balachandran, Coupling between high-frequency modes and a low-frequency mode: Theory and experiment, Nonlinear Dynam. 11 (1996) 17–36.

[3] H.N. Arafat, A.H. Nayfeh, C.-M. Chin, Nonlinear nonplanar dynamics of parametrically excited cantilever beams, Nonlinear Dynam. 15 (1998) 31–61.

[4] M. Colin, O. Thomas, S. Grondel, É. Cattan, Very large amplitude vibrations of flexible structures: Experimental identification and validation of a quadratic drag damping model, J. Fluids Struct. 97 (103056) (2020).

[5] É. Cottanceau, O. Thomas, P. Véron, M. Alochet, R. Deligny, A finite element/quaternion/asymptotic numerical method for the 3D simulation of flexible cables, Finite Elem. Anal. Des. 139 (2018) 14–34.

[6] D. Manfredo, V. Dörlich, J. Linn, M. Arnold, Data based constitutive modelling of rate independent inelastic effects in composite cables using preisach hysteresis operators, Multibody Syst. Dyn. (2023) http://dx.doi.org/10.1007/s11044-023-09910-y.

[7] O. Thomas, A. Sénéchal, J.F. Deü, Hardening/softening behaviour and reduced order modelling of nonlinear vibrations of rotating cantilever beams, Nonlinear Dyn. 86 (2) (2016) 1293–1318, http://dx.doi.org/10.1007/s11071-016-2965-0.

[8] W. Su, C.E.S. Cesnik, Strain-based geometrically nonlinear beam formulation for modeling very flexible aircraft, Int. J. Solids Struct. 48 (2011) 2349–2360.

[9] R. Alcorta, B. Chouvion, G. Michon, O. Montagnier, On the use of frictional dampers for flutter mitigation of a highly flexible wing, Int. J. Non-Linear Mech. 156 (104515) (2023) http://dx.doi.org/10.1016/j.ijnonlinmec.2023.104515.

[10] A. Martin, A. Opreni, A. Vizzaccaro, M. Debeurre, L. Salles, A. Frangi, O. Thomas, C. Touzé, Reduced order modeling of geometrically nonlinear rotating structures using the direct parametrisation of invariant manifolds, J. Theoret., Comput. Appl. Mech. (2023) http://dx.doi.org/10.46298/jtcam.10430.

[11] P. Vincent, A. Descombin, S. Dagher, T. Seoudi, A. Lazarus, O. Thomas, A. Ayari, S.T. Purcell, S. Perisanu, Nonlinear polarization coupling in freestanding nanowire/nanotube resonators, J. Appl. Phys. 125 (044302) (2019).

[12] A. Givois, J.-F. Deü, O. Thomas, Dynamics of piezoelectric structures with geometric nonlinearities: A non-intrusive reduced order modelling strategy, Comput. Struct. 253 (106575) (2021).

[13] V. Guillot, A. Givois, M. Colin, O. Thomas, A.T. Savadkoohi, C.-H. Lamarque, Theoretical and experimental investigation of a 1:3 internal resonance in a beam with piezoelectric patches, J. Vib. Control 26 (13–14) (2020) 1119–1132, http://dx.doi.org/10.1177/1077546320910536.

[14] S. Leadenham, A. Erturk, Unified nonlinear electroelastic dynamics of a bimorph piezoelectric cantilever for energy harvesting, sensing, and actuation, Nonlinear Dynam. 79 (2015) 1727–1743.

[15] Z. Yang, A. Erturk, J. Zu, On the efficiency of piezoelectric energy harvesters, Extreme Mech. Lett. 15 (2017) 26–37.

[16] L.N. Virgin, S.T. Santillian, R.H. Plaut, Vibration isolation using extreme geometric nonlinearity, J. Sound Vib. 315 (2008) 721–731.

[17] P. Carré, J. Bensoam, Sound synthesis of a 3D nonlinear string using a covariant Lie group integrator of a geometrically exact beam model, J. Sound Vib. 544 (2023) 117354.

[18] M. Debeurre, A. Grolet, B. Cochelin, O. Thomas, Finite element computation of nonlinear modes and frequency response of geometrically exact beam structures, J. Sound Vib. 548 (2023) 117534.

[19] M. Debeurre, A. Grolet, O. Thomas, Extreme nonlinear dynamics of cantilever beams: effect of gravity and slenderness on the nonlinear modes, Nonlinear Dynam. 111 (2023) 12787–12815, http://dx.doi.org/10.1007/s11071-023-08637-x.

[20] H. Farokhi, M.H. Ghayesh, Geometrically exact extreme vibrations of cantilevers, Int. J. Mech. Sci. 168 (2020) 105051.

[21] H. Farokhi, Y. Xia, A. Erturk, Experimentally validated geometrically exact model for extreme nonlinear motions of cantilevers, Nonlinear Dyn. 107 (457–475) (2022).

[22] J.P. Cusumano, F.C. Moon, Chaotic non-planar vibrations of the thin elastica, Part II: Derivation and analysis of a low-dimensional model, J. Sound Vib. 179 (2) (1995) 209–226.

[23] T.J. Anderson, B. Balachandran, A.H. Nayfeh, Nonlinear resonances in a flexible cantilever beam, J. Vib. Acoust. 116 (4) (1994) 480–484, http://dx.doi.org/10.1115/1.2930452.

[24] M. Tabaddor, A.H. Nayfeh, An experimental investigation of multimode responses in a cantilever beam, Trans. ASME 119 (1997) 532–538.

[25] P. Malatkar, A.H. Nayfeh, On the transfer of energy between widely spaced modes in structures, Nonlinear Dynam. 31 (2003) 225–242.

[26] H. Farokhi, E. Kohtanen, A. Erturk, Extreme parametric resonance oscillations of a cantilever: An exact theory and experimental validation, Mech. Syst. Signal Process. 196 (2023) 110342.

[27] G. Kerschen, M. Peeters, J.C. Golinval, A.F. Vakakis, Nonlinear normal modes, Part I: A useful framework for the structural dynamicist, Mech. Syst. Signal Process. 23 (1) (2009) 170–194.

[28] S. Shaw, C. Pierre, Nonlinear normal modes and invariant manifolds, J. Sound Vib. 150 (1) (1991) 170–173.

[29] C. Touzé, O. Thomas, A. Chaigne, Hardening/softening behaviour in non-linear oscillations of structural systems using non-linear normal modes, J. Sound Vib. 273 (1–2) (2004) 77–101, http://dx.doi.org/10.1016/j.jsv.2003.04.005.

[30] C. Touzé, A. Vizzaccaro, O. Thomas, Model order reduction methods for geometrically nonlinear structures: A review of nonlinear techniques, Nonlinear Dynam. 105 (2021) 1141–1190, http://dx.doi.org/10.1007/s11071-021-06693-9.

[31] M. Peeters, R. Viguié, G. Sérandour, G. Kerschen, J.-C. Golinval, Nonlinear normal modes, Part II: Toward a practical computation using numerical continuation techniques, Mech. Syst. Signal Process. 23 (2009) 195–216.

[32] L. Renson, G. Kerschen, B. Cochelin, Numerical computation of nonlinear normal modes in mechanical engineering, J. Sound Vib. 364 (2016) 177–206.

[33] M. Peeters, G. Kerschen, J.C. Golinval, Dynamic testing of nonlinear vibrating structures using nonlinear normal modes, J. Sound Vib. 330 (2011) 486–509.

[34] V. Denis, M. Jossic, C. Giraud-Audine, B. Chomette, A. Renault, O. Thomas, Identification of nonlinear modes using phase-locked-loop experimental continuation and normal form, Mech. Syst. Signal Process. 106 (2018) 430–452, http://dx.doi.org/10.1016/j.ymssp.2018.01.014.

[35] M. Scheel, S. Peter, R.I. Leine, M. Krack, A phase resonance approach for modal testing of structures with nonlinear dissipation, J. Sound Vib. 435 (2018) 56–73.

[36] L. Renson, A. Gonzalez-Buelga, D.A.W. Barton, S.A. Neild, Robust identification of backbone curves using control-based continuation, J. Sound Vib. 367 (2016) 145–158, http://dx.doi.org/10.1016/j.jsv.2015.12.035.

[37] M. Volvert, G. Kerschen, Phase resonance nonlinear modes of mechanical systems, J. Sound Vib. 511 (2021) 116355, http://dx.doi.org/10.1016/j.jsv.2021.116355.

[38] M. Jossic, B. Chomette, V. Denis, O. Thomas, A. Mamou-Mani, D. Roze, Effects of internal resonances in the pitch glide of Chinese gongs, J. Acoust. Soc. Am. 144 (1) (2018) 431–442, http://dx.doi.org/10.1121/1.5038114.

[39] S. Peter, R.I. Leine, Excitation power quantities in phase resonance testing of nonlinear systems with phase-locked-loop excitation, Mech. Syst. Signal Process. 96 (2017) 139–158.

[40] G. Abeloos, F. Müller, E. Ferhatoglu, M. Scheel, C. Collette, G. Kerschen, M.R.W. Brake, P. Tiso, L. Renson, M. Krack, A consistency analysis of phase-locked-loop testing and control-based continuation for a geometrically nonlinear frictional system, Mech. Syst. Signal Process. 170 (2022) 108820.

[41] A. Givois, J.-J. Tan, C. Touzé, O. Thomas, Backbone curves of coupled cubic oscillators in one-to-one internal resonance: bifurcation scenario, measurements and parameter identification, Meccanica 55 (2020) 481–503, http://dx.doi.org/10.1007/s11012-020-01132-2.

[42] A. Givois, C. Giraud-Audine, J.-F. Deü, O. Thomas, Experimental analysis of nonlinear resonances in piezoelectric plates with geometric nonlinearities, Nonlinear Dynam. 102 (2020) 1451–1462, http://dx.doi.org/10.1007/s11071-020-05997-6.

[43] M. Krack, Nonlinear modal analysis of nonconservative systems: Extension of the periodic motion concept, Comput. Struct. 154 (2015) 59–71.

[44] D. Laxalde, F. Thouverez, Complex non-linear modal analysis for mechanical systems application to turbomachinery bladings with friction interfaces, J. Sound Vib. 322 (4–5) (2009) 1009–1025.

[45] J. Sieber, B. Krauskopf, Control based bifurcation analysis for experiments, Nonlinear Dynam. 51 (2008) 365–377.

[46] D.W. Barton, S.G. Burrow, Numerical continuation in a physical experiment: Investigation of a nonlinear energy harvester, J. Comput. Nonlinear Dyn. (2011) 11010.

[47] E. Bureau, F. Schilder, M. Elmegård, I.F. Santos, J.J.T.J. Starke, Experimental bifurcation analysis of an impact oscillator - determining stability, J. Sound Vib. 333 (2014) 5464–5474.

[48] M. Géradin, A. Cardona, Flexible Multibody Dynamics: A Finite Element Approach, John Wiley & Sons, Ltd, Chichester, 2001.

[49] G. Genta, Vibration Dynamics and Control, Springer, 2009.

[50] W. Lacarbonara, H. Yabuno, Refined models of elastic beams undergoing large in-plane motions: Theory and experiment, Int. J. Solids Struct. 43 (2006) 5066–5084.

[51] A. Lazarus, O. Thomas, J.-F. Deü, Finite elements reduced order models for nonlinear vibrations of piezoelectric layered beams with applications to NEMS, Finite Elem. Anal. Des. 49 (1) (2012) 35–51, http://dx.doi.org/10.1016/j.finel.2011.08.019.

[52] C. Touzé, O. Thomas, A. Chaigne, Asymmetric non-linear forced vibrations of free-edge circular plates, part 1: theory, J. Sound Vib. 258 (4) (2002) 649–676, http://dx.doi.org/10.1006/jsvi.2002.5143.

[53] O. Thomas, C. Touzé, A. Chaigne, Non-linear vibrations of free-edge thin spherical shells: modal interaction rules and 1:1:2 internal resonance, Int. J. Solids Struct. 42 (11–12) (2005) 3339–3373, http://dx.doi.org/10.1016/j.ijsolstr.2004.10.028.

[54] M. Amabili, Nonlinear Vibrations and Stability of Shells and Plates, Cambridge University Press, 2008.

[55] B. Audoly, S. Neukirch, A one-dimensional model for elastic ribbons: A little stretching makes a big difference, J. Mech. Phys. Solids 153 (2021) 194457.

[56] M.R.M. Crespo da Silva, C.C. Glynn, Nonlinear flexural-flexural-torsional dynamics of inextensible beams. I. equations of motion, J. Struct. Mech. 6 (1978) 437–448.

[57] A. Vizzaccaro, A. Givois, P. Longobardi, Y. Shen, J.-F. Deü, L. Salles, C. Touzé, O. Thomas, Non-intrusive reduced order modelling for the dynamics of geometrically nonlinear flat structures using three dimensional finite elements, Comput. Mech. 66 (2020) 1293–1319, http://dx.doi.org/10.1007/s00466-020-01902-5.

[58] A. Vizzaccaro, A. Opreni, L. Salles, A. Frangi, C. Touzé, High order direct parametrisation of invariant manifolds for model order reduction of finite element structures: application to large amplitude vibrations and uncovering of a folding point, Nonlinear Dynam. 110 (2022) 525–571.

[59] M. Vakilinejad, A. Grolet, O. Thomas, A comparison of robustness and performance of linear and nonlinear lanchester dampers, Nonlinear Dyn. 100 (2020) 269–287, http://dx.doi.org/10.1007/s11071-020-05512-x.

[60] M. Amabili, Nonlinear damping in nonlinear vibrations of rectangular plates: Derivation from viscoelasticity and experimental validation, J. Mech. Phys. Solids 118 (2018) 275–292.

[61] S. Leadenham, A. Erturk, Unified nonlinear electroelastic dynamics of a bimorph piezoelectric cantilever for energy harvesting, sensing, and actuation, Nonlinear Dynam. 79 (2015) 1727–1743.

[62] R.M. Rosenberg, The normal mode of n-degree-of-freedom systems, J. Appl. Mech. 33 (4) (1962) 877–880.

[63] C. Touzé, M. Amabili, Nonlinear normal modes for damped geometrically nonlinear systems: Application to reduced-order modelling of harmonically forced structures., J. Sound Vib. 298 (4–5) (2006) 958–981.

[64] L. Renson, G. Deliège, G. Kerschen, An effective finite-element-based method for the computation of nonlinear normal modes of nonconservative systems, Meccanica 49 (2014) 1901–1916.

[65] A. Liapounoff, Problème général de la stabilité du mouvement, Ann. Fac. Sci. Univ. Toulouse 9 (2) (1907) 203–474.

[66] A. Kelley, On the liapunov subcenter manifold, J. Math. Anal. Appl. 18 (1967) 472–478.

[67] R. de la Llave, F. Kogelbauer, Global persistence of Lyapunov subcenter manifolds as spectral submanifolds under dissipative perturbations, SIAM J. Appl. Dyn. Syst. 18 (4) (2019) 2099–2142.

[68] G. Haller, S. Ponsioen, Nonlinear normal modes and spectral submanifolds: existence, uniqueness and use in model reduction, Nonlinear Dynam. 86 (2016) 1493–1534.

[69] M. Cenedese, G. Haller, How do conservative backbone curves perturb into forced responses? A melnikov function analysis, Proc. R. Soc. Lond. Ser. A Math. Phys. Eng. Sci. 476 (2020) 20190494.

[70] Z.A. Shami, Y. Shen, C. Giraud-Audine, C. Touzé, O. Thomas, Nonlinear dynamics of coupled oscillators in 1:2 internal resonance: effects of the non-resonant quadratic terms and recovery of the saturation effect, Meccanica 57 (2022) 2701–2731, http://dx.doi.org/10.1007/s11012-022-01566-w.

[71] C. Grenat, Nonlinear Normal Modes and Multi-Parametric Continuation of Bifurcations : Application to Vibration Absorbers and Architectured MEMS sensors for mass detection (Ph.D. thesis), Lyon university, INSA, France, 2019, http://theses.insa-lyon.fr/publication/2018LYSEI078/these.pdf.

[72] S. Giclais, P. Lubrina, C. Stephan, Aircraft ground vibration testing at ONERA, Aerosp. Lab J. 12 (2016) AL12–15, http://dx.doi.org/10.12762/2016.AL12-05.

[73] S. Mojrzisch, J. Wallaschek, J. Bremer, An experimental method for the phase controlled frequency response measurement of nonlinear vibration systems, Proc. Appl. Math. Mech. 12 (1) (2012) 253–254.

[74] A. Opreni, A. Vizzaccaro, C. Touzé, A. Frangi, High-order direct parametrisation of invariant manifolds for model order reduction of finite element structures: application to generic forcing terms and parametrically excited systems, Nonlinear Dynam. 111 (2023) 5401–5447.

[75] M. Peeters, G. Kerschen, J. Golinval, Modal testing of nonlinear vibrating structures based on nonlinear normal modes: Experimental demonstration, Mech. Syst. Signal Process. 25 (4) (2011) 1227–1247.

[76] S. Peter, F. Schreyer, R.I. Leine, A method for numerical and experimental nonlinear modal analysis of nonsmooth systems, Mech. Syst. Signal Process. 120 (2019) 193–807.

[77] S.S.L. Kohlmann, A. Hartung, J. Gross, M. Scheel, M. Krack, Validation of a turbine blade component test with frictional contacts by phase-locked-loop and force-controlled measurements, J. Eng. Gas Turbines Power 142 (2020) 051006.

[78] F. Müller, L. Woiwode, J. Gross, M. Scheel, M. Krack, Nonlinear damping quantification from phase-resonant tests under base excitation, Mech. Syst. Signal Process. 177 (2022) 109170.

[79] L. Renson, T.L. Hill, D.A. Ehrhardt, D.A.W. Barton, S.A. Neild, Force appropriation of nonlinear structures, Proc. R. Soc. Lond. Ser. A Math. Phys. Eng. Sci. 474 (20170880) (2018).

[80] D.A. Ehrhardt, M.S. Allen, Measurement of nonlinear normal modes using multi-harmonic stepped force appropriation and free decay, Mech. Syst. Signal Process. 76–77 (2016) 612–633.

[81] M. Scheel, T. Weigele, M. Krack, Challenging an experimental nonlinear modal analysis method with a new strongly friction-damped structure, J. Sound Vib. 485 (2020) 115580.

[82] P. Viguié, C. Vergez, S. Karkar, B. Cochelin, Regularized friction and continuation: Comparison with Coulomb'slaw, J. Sound Vib. 389 (2017) 350–363.

[83] S. Benacchio, C. Giraud-Audine, O. Thomas, Effect of dry friction on a parametric non linear oscillator, Nonlinear Dynam. 108 (2022) 1005–1026, http://dx.doi.org/10.1007/s11071-022-07233-9.

[84] S.A.N. J. M. Londoño and, J.E. Cooper, Identification of backbone curves of nonlinear systems from resonance decay responses, J. Sound Vib. (2015).

[85] R. Arquier, S. Bellizzi, R. Bouc, B. Cochelin, Two methods for the computation of nonlinear modes of vibrating systems at large amplitude, Comput. Struct. 84 (2006) 1565–1576.

[86] F.J. Munoz-Almaraz, E. Freire, J. Galán, E. Doedel, A. Vanderbauwhede, Continuation of periodic orbits in conservative and Hamiltonian systems, Physica D 181 (1–2) (2003) 1–38.

[87] F. Alijani, M. Amabili, P. Balasubramanian, S. Carra, G. Ferrari, R. Garziera, Damping for large-amplitude vibrations of plates and curved panels, Part 1: Modeling and experiments, Int. J. Non-Linear Mech. 85 (2016) 23–40, http://dx.doi.org/10.1016/j.ijnonlinmec.2016.05.003.

[88] M. Amabili, F. Alijani, J. Delannoy, Damping for large-amplitude vibrations of plates and curved panels, Part 2: Identification and comparisons, Int. J. Non-Linear Mech. 85 (2016) 226–240, http://dx.doi.org/10.1016/j.ijnonlinmec.2016.05.004.

[89] M. Amabili, Nonlinear damping in large-amplitude vibrations: modelling and experiments, Nonlinear Dynam. 93 (2018) 4–18.

[90] M. Amabili, Derivation of nonlinear damping from viscoelasticity in case of nonlinear vibrations, Nonlinear Dynam. 97 (2019) 1785–1797, http://dx.doi.org/10.1007/s11071-018-4312-0.

[91] M. Amabili, P. Balasubramanian, G. Ferrari, Nonlinear vibrations and damping of fractional viscoelastic rectangular plates, Nonlinear Dynam. 103 (2021) 3581–3609.

[92] Basler, Basler video recording software, 2021, https://www2.baslerweb.com/en/downloads/software-downloads/. (Accessed 26 January 2021).

[93] T. Hendrick, Dltdv digitizing tool: MATLAB tools for digitizing video files and calibrating cameras, 2022, https://biomech.web.unc.edu/dltdv/. (Accessed 9 March 2022).

[94] M. Géradin, D. Rixen, Mechanical Vibrations, Theory and Application to Structural Dynamics, Wiley, New York, 2015.

[95] X. Sun, G. Kerschen, L. Cheng, Geometrical nonlinearities in a curved cantilever beam: A condensation model and inertia-induced nonlinear features, Nonlinear Dynam. 111 (2023) 6533–6556.

[96] W. Young, R. Budynas, Roark's Formulas for Stress and Strain, 7th, McGraw Hill, 2002.

[97] R.T. Shield, Bending of a beam or a wide strip, Q. J. Mech. Appl. Math. 45 (1992) 567–573.

[98] S.A. Nayfeh, A.H. Nayfeh, Nonlinear interactions between two widely spaced modes - external excitation, Int. J. Bifurc. Chaos 3 (2) (1993) 417–427.

[99] A. Chaigne, C. Lambourg, Time-domain simulation of damped impacted plates, J. Acoust. Soc. Am. 109 (4) (2001) 1422–1432.

[100] B. Chouvion, S. McWilliam, A.A. Popov, C.H.J. Fox, Review and comparison of different support loss models for micro-electro-mechanical systems resonators undergoing in-plane vibration, Proc. Inst. Mech. Eng. C 226 (1) (2012) 283–295.

[101] B. Peeters, G. Lowet, H.V. der Auweraer, J. Leuridan, A new procedure for modal parameter estimation, Sound Vib. 38 (1) (2004) 24–28.

[102] G. Gatti, C. Svelto, Exploiting nonlinearity for the design of linear oscillators: Application to an inherently strong nonlinear X-shaped-spring suspension, Mech. Syst. Signal Process. 197 (2023) 110362.

[103] M.H. Ghayesh, H. Farokhi, Extremely large dynamics of axially excited cantilevers, Thin Walled Struct. 154 (2020) 106275.

[104] L. Guillot, A. Lazarus, O. Thomas, C. Vergez, B. Cochelin, A purely frequency based floquet-hill formulation for the efficient stability computation of periodic solutions of ordinary differential systems, J. Comput. Phys. 416 (2020) 109477, http://dx.doi.org/10.1016/j.jcp.2020.109477.